Petroleum Science 23 (2026) 541–562

Contents lists available at ScienceDirect

Petroleum Science

journal homepage: www.keaipublishing.com/en/journals/petroleum-science

Original Paper

Fracture response patterns in deep to ultra-deep tight sandstones: A comparison based on core and borehole images

Yu Du [a], Hu-Cheng Deng [a,b,*], Xiao-Fei Hu [a,b], Hao-Tian Zhang [c], Hong-Hui Wang [a], Cui-Li Wang [d], Mao-Xin Liu [a], Chen-Yang Zhao [a], Shang-Rong Guo [a], Zi-Yun Zheng [a]

[a] College of Energy (College of Modern Shale Gas Industry), Chengdu University of Technology, Chengdu, 610059, Sichuan, China
[b] State Key Laboratory of Oil and Gas Reservoir Geology, Chengdu University of Technology, Chengdu, 610059, Sichuan, China
[c] Department of Quality Management and Inspection Testing, Yibin University, Yinbin, 644000, Sichuan, China
[d] PetroChina Tarim Oilfield Company, Korla, 841000, Xinjiang, China

ARTICLE INFO

Article history:
Received 12 May 2025
Received in revised form
9 September 2025
Accepted 11 September 2025
Available online 17 September 2025

Edited by Xi Zhang and Jie Hao

Keywords:
Borehole images
Natural fracture
Fracture image features
Fracture response pattern
Fracture identification
Tight sandstone reservoir

ABSTRACT

Natural fractures serve as the primary storage spaces and flow pathways in deep to ultra-deep tight sandstone reservoirs, directly influencing hydrocarbon accumulation, preservation, and production. Borehole images offer intuitive, continuous, and high-resolution identification of natural fractures along the entire borehole. However, relying solely on complete sinusoidal curves from borehole images for fracture identification may lead to omissions, as it overlooks cases where these curves are incomplete or truncated. To address the problems and deficiencies in fracture identification, this study systematically classifies borehole image feature patterns based on core-to-log spatial position restoring. A bidirectional comparison is conducted between natural fractures in cores and the fracture image features in borehole images. A quantitative relationship between fracture dip angle, thin layer thickness and borehole radius was established, accompanied by a mathematical expression describing the fracture curve morphology was proposed. These findings enabled the development of an imaging response pattern for natural fractures in deep and ultra-deep tight sandstone reservoirs, incorporating key parameters such as dip angle, through-layer connectivity, and spatial position within the borehole. In the Bashijiqike–Baxigai tight-sandstone reservoirs of the Bozi–Dabei area, we estimate that approximately 24% of core-observed fractures display distinct linear-pattern features on borehole images, whereas approximately 91% of borehole images features can be correlated with fractures observed in core. Fracture identification rates for natural fractures increased by 17% in water-based mud and by 3% in oil-based mud through the application of the natural fracture image response pattern. Moreover, this study analyzes the deviations in the matching between core fractures and image features. Finally, we further discuss the common sources of error in natural fracture identification using borehole images from multiple perspectives, including missing core responses, inconsistencies between core and borehole image features, distortion of fracture chord curve, inaccurate fracture count, misclassification of fractures, and variations in interpretation under different mud systems. The research addresses the blind spots of traditional methods in fracture identification within thin layers, not only enhancing the detection rate of natural fractures but also further improving the accuracy of fracture recognition. At the same time, it will contribute to the optimization of fracture characterization, reservoir evaluation, and production forecasting, providing a more reliable data foundation for exploration and development under complex geological conditions.

1. Introduction

Borehole images is a logging technique that generates high-resolution, two-dimensional images around the borehole, utilizing the differences in the electrical or acoustic properties (Genter

* Corresponding author.
E-mail address: denghucheng@cdut.edu.cn (H.-C. Deng).
Peer review under the responsibility of China University of Petroleum (Beijing).

https://doi.org/10.1016/j.petsci.2025.09.021

et al., 1997; Goldberg, 1997; Massiot et al., 2015; Lai et al., 2018). Borehole images is referred to as the “underground microscope” for geologists (Lai et al., 2024b), with the highest vertical resolution (5 mm) and borehole coverage (Lofts et al., 1998; Folkestad et al., 2012). These images can clearly display geological features such as lithology, stratification, cavities, and fractures on the images (Prensky, 1999; Sun et al., 2006; Gaillot et al., 2007). Borehole images has unique advantages, especially in the identification of natural fractures, and can identify and quantitatively evaluate features such as fracture orientation, effectiveness, geometric parameters, and development patterns.

To adapt to more complex geological conditions, borehole images fracture identification technology has continuously evolved in the petroleum industry (Ekstrom et al., 1986; Safinya et al., 1991; Prensky, 1999; Chitale et al., 2004; Kalathingal et al., 2010; Laronga et al., 2011; Lai et al., 2024b). Numerous scholars have systematically elucidated the response characteristics of various fracture types through comparisons between core and borehole images (MacLeod et al., 1992; Genter et al., 1997; Paulsen et al., 2002; Qu et al., 2016; Qi et al., 2025). At the same time, some scholars have explored the detection limit of fracture scale in borehole images through experimental testing and response simulations (Lai et al., 2017; Li et al., 2025b). Researchers have employed various image enhancement techniques to improve the quality of borehole images and the ability to recognize fracture features. These techniques include histogram equalization, two-dimensional discrete wavelet transform, Retinex algorithm, morphing technology, nonlocal means denoising, and adaptive contrast enhancement (Yan et al., 2006; Zhang et al., 2012; Wu et al., 2016; Fu, 2020). However, due to the spacing between electrodes in electrical borehole images, blank stripes inevitably appear in the images, increasing the uncertainty in fracture identification. Many researchers have focused on optimizing the filling of blank strips using traditional interpolation methods such as Criminisi and Filtersim algorithms, (Ballester et al., 2001; Hurley et al., 2011; Yamada et al., 2013; Li et al., 2017b), as well as deep learning techniques like Encoder-Decoder, U-Net, and GAN (Rumelhart et al., 1985; Goodfellow et al., 2014; Wang et al., 2019; Chen et al., 2021; Dong et al., 2022; Yuan et al., 2022), in order to address this issue. Moreover, the identification of fractures remains heavily dependent on interpreter expertise, resulting in a complex and time-intensive workflow (Liu et al., 2013; Pan et al., 2018; Du et al., 2023). Automated fracture identification techniques based on borehole images are increasingly replacing manual interpretation, thereby enhancing the efficiency of fracture detection. This technology has evolved from traditional computer vision methods, such as Hough transform, edge detection, thresholding, and mathematical morphology (Hall et al., 1996; Qi, 2005; Xavier et al., 2015; Shafiabadi et al., 2021). It has now advanced to deep learning-based intelligent recognition techniques, including YOLOv5, Fast R-CNN, and Mask R-CNN (Du et al., 2023; Han et al., 2023; Azizzadeh Mehmandost Olya et al., 2024), continuously improving the precision and efficiency of fracture identification.

Regardless of the method used for fracture identification in borehole images, it essentially relies on the image features formed on the imaging unfold diagram after the fractures intersect the borehole (Qin et al., 2000; Wang et al., 2025). In general, when fractures intersect the cylindrical borehole, their image traces typically appear as characteristic chord curves (Prensky, 1999). The color, continuity, and morphological characteristics of the chord curve, directly reflect key information on the fracture's attitude, effectiveness, and other key characteristics (Deng et al., 2013; Liu, 2013).

Although chord curve features have been widely applied in fracture identification, some image features of fractures under special conditions remain unclear (Luo et al., 2023; Gong et al., 2024). In complex cases—such as when fractures are perpendicular to the borehole, do not fully cut through the borehole, are constrained by lithologic interfaces, developed within interlayers, or when the borehole becomes elliptical—the typical chord curve may no longer hold (Fernandez-Ibanez et al., 2018; Lai et al., 2022b; Cao et al., 2024). These cases lead to the absence or distortion of chord curve, or to the appearance of fracture images that do not follow the chord pattern. As a result, the difficulty of fracture identification is significantly increased. Moreover, factors such as the resolution of borehole images, borehole wall flushing effects, fracture fillings, and the interaction between the instrument and the borehole can all affect the imaging of fractures. This further leads to discrepancies between the core fracture characteristics and the fracture image features from borehole images (Zeng et al., 2023a; Zhao et al., 2024). Current understanding of the imaging response mechanisms of complex or incomplete fractures remains insufficient. In addition, the fracture identification process lacks unified and practical interpretation standards and methodological frameworks. This has become one of the key bottlenecks limiting further improvements in fracture identification accuracy.

As one of the most crucial foundational data sources for fracture studies, borehole images directly reveal the scale and characteristics of natural fracture development. It plays an irreplaceable role in fracture identification and characterization, fracture effectiveness evaluation, and reservoir fracture system modeling (Olson et al., 2009; Zeng et al., 2022; Wood, 2024). To date, no image response pattern for borehole images has been established, that comprehensively considers features such as the dip angle, through-layer connectivity, and spatial position of natural fractures within the borehole. Therefore, it is necessary to further explore the fracture information contained in borehole images, and systematically analyze the imaging characteristics of various fracture types. It holds significant practical application value for improving the accuracy of fracture identification.

In this paper, we performed spatial alignment of the cores and observed the natural fracture characteristics in the core. A systematic classification of borehole images feature patterns was made based on color, morphology, curve identification ability, and geological significance. The core fractures and borehole images fracture features are precisely matched one-to-one through accurate bidirectional matching. We summarized the imaging characteristics of natural fractures with different features on borehole images. We established an image response pattern for natural fractures in deep and ultra-deep tight sandstone reservoirs, incorporating key parameters such as dip angle, through-layer connectivity, and spatial position within the borehole. The proposed pattern enables accurate identification of natural fractures using borehole images in intervals or wells lacking core data. Moreover, this study analyzes the deviations in the bidirectional matching between core fractures and image features. Additionally, we discuss the common sources of error in natural fracture identification using borehole images from multiple perspectives. The research further enriches and refine the foundation for fracture identification using borehole images, and offer significant guidance for oil and gas exploration and development practices.

2. Materials and methods

2.1. Geological background

The Kuqa Depression is a key area for oil and gas exploration and development in the Tarim Basin (Liu et al., 2019; Li et al.,

2025a). It borders the South Tianshan fold-and-thrust belt to the north and the North Tarim Uplift to the south, covering a total area of approximately 5500 km^2. The Kuqa Depression appears as a NE–SW elongated strip in the plane, wide in the central area and narrowing toward the east and west (Xu et al., 2022). The current structural pattern of the Kuqa Depression is divided into four belts and three depressions, comprising the Northern Monocline Belt, the Kelasu Structural Belt, the Wushi Depression, the Baicheng Depression, the Yangxia Depression, the Qiulitage Structural Belt, and the Southern Slope Belt (Fig. 1(a)) (Lin et al., 2002).

The Bozi-Dabei area, located in the western segment of the Kelasu Structural Belt, experienced sedimentation during the Early to Middle Cretaceous (Fig. 1(b)) (Liu, 2023). Controlled by the north-to-south thrusting of the South Tianshan orogeny during the Himalayan period, a series of NEE-trending thrust faults developed in the region (Fig. 1(b)) (Tang et al., 2006).

The main exploration and development target layer is the Lower Cretaceous Bashijiqike and Baxigai formations (Fig. 1(c)). The lithology is primarily composed of thick layers of medium–fine sandstone (Zhang et al., 2024). Burial depth ranges from 5300 to 7800 m, with an average measured porosity of 4.8% (Chen et al., 2024). It exhibits prominent characteristics of deep burial, ultra-low porosity and permeability, and firm heterogeneity. The Bashijiqike and Baxigai formations undergo multiple phases of tectonic events (Zhang et al., 2014; Zhu et al., 2019a; Zeng et al., 2023b). During the tectonic evolution, fracturing of formation forms complex natural fracture systems (Mitchell, 1995; Reber et al., 2015; Xue et al., 2021; Wang et al., 2023; Li et al., 2024). Eventually, a typical deep to ultra-deep fracture-type tight sandstone reservoir is formed.

2.2. Data

The data involved in this study were all obtained from the Bozi–Dabei area of the Kuche Depression, Tarim Basin. The dataset includes:

(1) A total of 272.68 m of core samples from 22 wells;
(2) Core fracture observation, including the top depth, bottom depth, and middle depth of the fracture on the core, dip angle, infilling traits, aperture, mechanical properties, through-layer connectivity, whether the fracture penetrates the borehole;
(3) Core scanning image (using a scanner to scan the closely fitted core surface, obtaining a 360° color image of the core surface with a resolution of up to 10 pixels per millimeter, with details as fine as 40 pixels per millimeter);
(4) The borehole images data included 12 wells drilled with a water-based mud environments and 8 wells drilled with an oil-based mud environments.

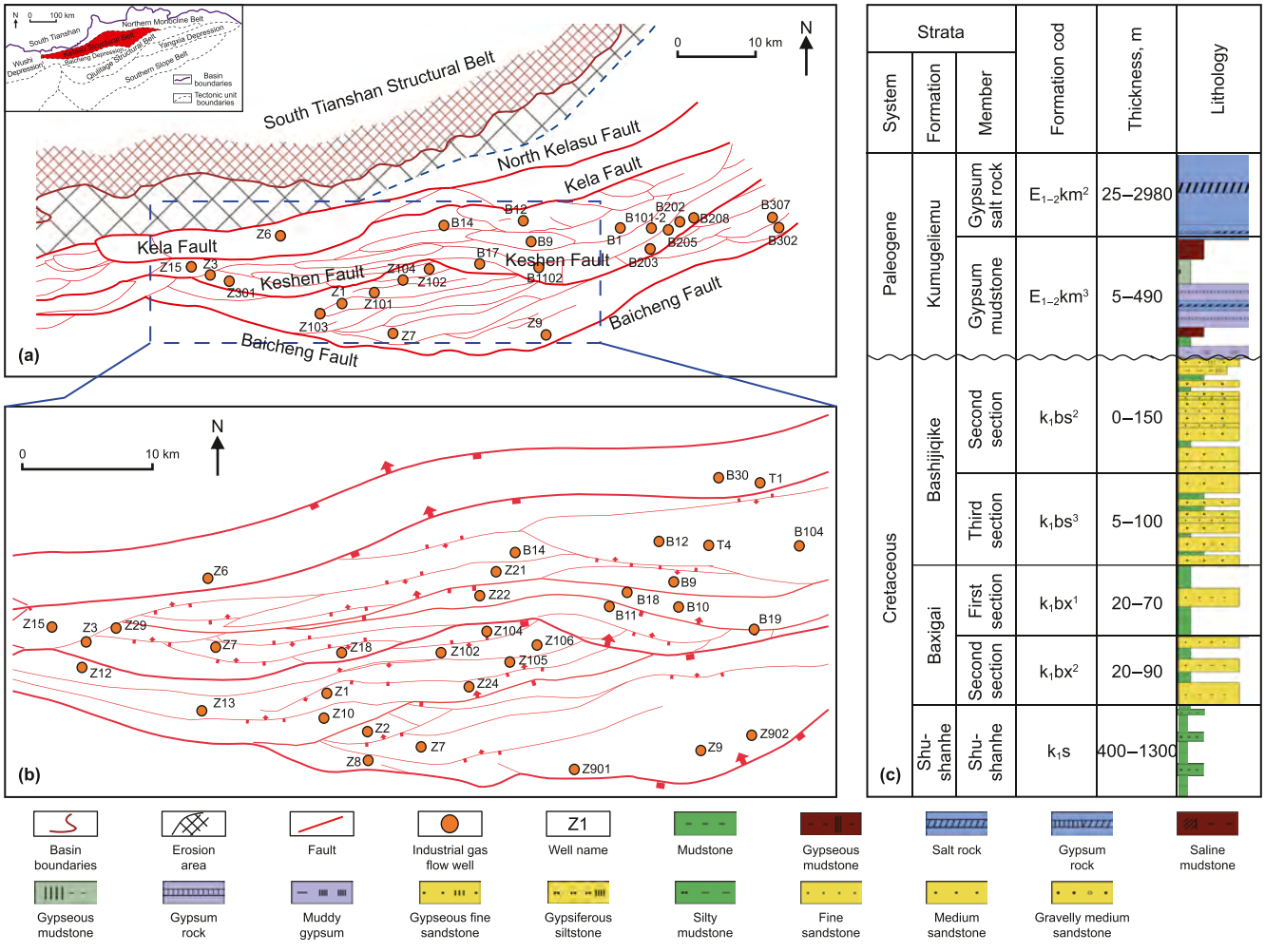

Fig. 1. Geological structures and stratigraphic background of the study area. **(a)** Structural unit division of the Kuqa Depression in the Tarim Basin. **(b)** Cretaceous top surface structure in the Bozi–Dabei area. **(c)** Stratigraphic column of the Bashijiqike–Baxigai Formation in the Lower Cretaceous (Wang et al., 2022a).

2.3. Methods

2.3.1. Core spatial position restoring

When both core data and full-interval borehole images are available for a well, there is inevitably a depth overlap between them. Therefore, the geological features observed from the cores in the overlapping intervals can be compared with the corresponding borehole image features (Fernandez-Ibanez et al., 2018). Through this method, the imaging responses of lithology, fractures, and special structures observed in cores can be identified on borehole images (Wang et al., 2014). However, core recovery rates typically fall short of 100%, and measurement errors in drill string length are common. As a result, the recorded depth of the core upon retrieval often deviates from the true depth indicated by borehole images (Li et al., 2020b). In addition, due to technical and cost limitations, non-oriented coring techniques are typically used, leading to the loss of the core's true orientation (Niu et al., 2005).

This study takes full advantage of borehole images, which offer high resolution, strong continuity, and intuitive accuracy. Geological features such as fractures and bedding observed in core images were compared with borehole images characteristics. First, the core intervals were corrected to their true subsurface depths, and subsequently, their actual underground orientations were restored (Li et al., 2017a).

2.3.1.1. Depth alignment of borehole images and core. Comparing core gamma measurements with wireline gamma logs is a widely adopted and effective method for core depth calibration. When cores are continuous and intact, this technique enables accurate and straightforward depth matching. However, in fractured reservoirs, cores are often fragmented and discontinuous, leading to considerable uncertainty in gamma-based calibration. To overcome this limitation, this study introduces a core scanning image stitching method that enables precise depth alignment even with discontinuous cores, thereby enhancing the accuracy of fracture identification and characterization.

Core scanning images are obtained by scanning the outer surface of the core (Zhang, 2013) (Fig. 2(a) and (b)), whereas borehole images provides a comprehensive scan of the entire borehole (Fig. 2(c)). Ignoring their size differences, the scale of the borehole images can be adjusted to align with that of the core scanning images (Fig. 2(b) and (c)). The core scanning images are stitched together in sequence by block number, from shallow to deep (Fig. 2(b)).

However, the core may exhibit physical damage or discontinuities caused by manual handling, interference from drilling tools, or a high density of natural fractures. In such cases, the top and bottom depths of the fragmented segment are determined based on the core description records. The fragmented segment is then left blank in the stitched image, skipping over that depth, and the sequence of continuous core images is continued.

To achieve spatial alignment, prominent geological features such as fractures and fracture networks, stratigraphic dip angles, lithological variations, and representative structures are first identified from the core. The corresponding geological features are then identified in the borehole images near the top and bottom depths of the core interval in the original record (Wang et al., 2014; Li et al., 2017a; Fernandez-Ibanez et al., 2018). Subsequently, the core images for the entire interval are shifted so that continuous geological features in the core align with those in the borehole images at identical depths. Next, the top and bottom depths of the fragmented segment are fine-tuned, thereby ensuring preliminary depth alignment between the core and borehole images.

2.3.1.2. Orientation alignment of borehole images and core. For non-oriented core sampling, logging personnel typically draw an marker line from the top to the base of the core (Zhu et al., 2019b) (Fig. 2(a)). Provided the core remains continuously intact, the marker line typically remains stable and all core intervals maintain consistent spatial orientation.

Following the preliminary core depth alignment, one of the geological features used for alignment were selected as the reference marker. Subsequently, the azimuth of the reference marker in the borehole images and its position on the core relative to the marker line was determined. Eq. (1) was then used to compute the true orientation of the core marker line. Finally, both the core images and borehole images were unified into a common coordinate system, each beginning at true north and arranged from left to right in the sequence N–E–S–W–N (Li et al., 2017a) (Fig. 2(a) and (b)).

$$\alpha = \frac{r}{l} \times 360^\circ \pm \beta \tag{1}$$

where α is the marker line orientation, °; r is the distance from the marker to the marker line, cm; l is the core circumference, cm; and β denotes the orientation of the reference marker, °. A + sign is used when the marker is to the right of the orientation line, and a – sign when it is to the left.

2.3.2. Core fracture observation

Core fractures were observed and measured to obtain characteristic parameters, including fracture aperture, infilling traits, through-layer connectivity, and mechanical properties.

Based on the known orientation of the core marker line, the orientations of fractures in each coring interval are inferred. On the core scanning image, the trough of the chord curve of each fracture is designated as the reference marker, and its orientation represents the fracture's trend (Yao et al., 2011). By back-calculating the orientation β of the reference marker using Eq. (1), the fracture trend is determined.

2.3.3. Classification of image feature patterns in borehole images

In borehole images, the response characteristics of core lithology, depositional features, fractures, and other geological structures were clarified. Borehole images image feature patterns were systematically summarized and classified based on color combination characteristics, morphological traits, chord-curve identification ability, and their geological significance, drawing on existing scholarly research and the author's practical experience (Li et al., 2009; Lai et al., 2018).

Classification of borehole images feature patterns adheres to two guiding principles—scientific rigor and practicality (You et al., 2000; Zhong et al., 2018). Scientific rigor requires that each feature type is underpinned by strict definitional criteria to avoid redundancy and ensure a comprehensive taxonomy. Additionally, each classified pattern must exhibit explicit geological significance to guarantee its validity and accuracy. Practicality demands that the classification methodology be straightforward and transparent, facilitating its practical application and dissemination. Enabling researchers to efficiently and accurately identify and categorize image features.

To facilitate subsequent investigation of core fractures and borehole images fracture features, and to ensure independent analysis of fracture information from each data source. We classified borehole images feature patterns into two primary categories: line patterns and non-line patterns. This classification framework enables line patterns to accurately represent fracture

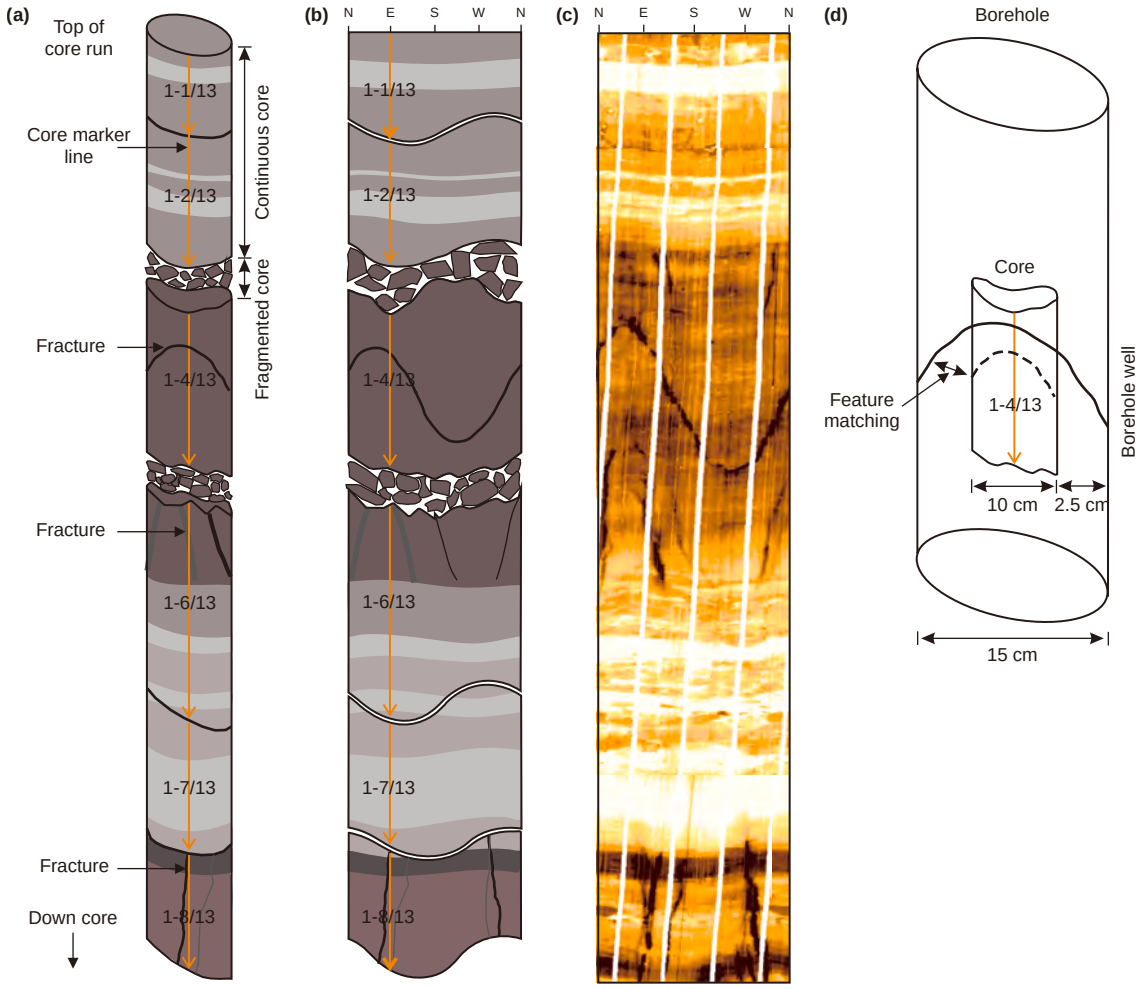

Fig. 2. Schematic comparison of core stitching and borehole images features. **(a)** Core sample schematic. **(b)** Schematic of core scanning image stitching. **(c)** Borehole images matched to the depth interval of the core. **(d)** Comparative schematic of fracture features between the core and borehole images.

characteristics in later studies, avoiding confusion with other geological features. It lays the groundwork for in-depth bidirectional comparison between core fractures and borehole images fracture features.

2.3.4. Bidirectional comparison of core fractures and fracture features

This study employs a bidirectional validation approach, using both "core to borehole images" and "borehole images to core" verification. Matching the fracture parameters observed in the core (such as dip angle, infilling traits, mechanical properties, through-layer connectivity, and spatial position within the borehole) with the corresponding image features in the line pattern of the borehole images. On the other hand, fracture image features in the borehole images are also traced back to the core, comparing their physical morphology and spatial position. The bidirectional comparison approach not only ensures high consistency and reliability between the two data sources in fracture response, but also minimizes missed detections and misidentifications to the greatest extent possible.

The orientation of fracture image features in borehole images can be obtained by fitting chord curves using fracture interpretation software. The type of drilling mud significantly influences the appearance of natural fractures in the borehole images (Chen et al., 2024). In water-based mud drilling, when fractures are filled with high-conductivity materials such as mud or clay, the image appears darker compared to the surrounding rock (Wang et al., 2022b). In oil-based mud drilling, when fractures are filled with low-conductivity materials such as mud, calcite, or quartz, the images appear brighter compared to the surrounding rock (Lai et al., 2017).

When the orientation and infilling of the core fractures match the image features and core fractures depth intervals fall within the depth range indicated by the image features, it can be initially determined that they correspond to the same fracture (Fig. 2(d)). If fractures are clearly observed in the core but no corresponding image response, or if fracture images are clearly shown in the borehole images but no corresponding fractures are present in the core, a depth discrepancy analysis should be conducted.

It is important to note that the core diameter is typically 8 cm or 10 cm, while the average borehole diameter is 15 cm. The imaging range of borehole images is wider than the core, by approximately 5–7 cm (Khoshbakht et al., 2012) (Fig. 2(d)). Core fractures extend into the borehole wall in three-dimensional space, causing a mismatch in the top and bottom depths of the fractures between the core and borehole images. Therefore, spatial extend factors must be fully considered when matching fracture information. Although there is a certain gap between the core and the borehole wall, it usually does not affect the calibration of geological features between the core and borehole images (Nian et al., 2021).

2.3.5. Establishing natural fracture image response pattern

Clarify the image features of natural fractures on the borehole images unfolding, based on the dip angle, through-layer connectivity, and spatial position within the borehole. Establish an image response pattern for natural fractures in borehole images. The proposed pattern enables accurate identification of natural fractures using borehole images in intervals or wells lacking core data.

3. Results

3.1. Core spatial position restoring

The first-pass core scanning image of well Z104 was processed through stitching and aligned with the corresponding borehole images at the same vertical scale (Fig. 3(a) and (b)). Select typical fracture intersection markers on the core (indicated by green circles) and their corresponding positions in the borehole images (Fig. 3(c)). This confirms that the depth of the continuous core below the fragmented segment has been properly realigned. Next, select the intersection of lithological interfaces and fracture of the continuous core above the fragmented segment as reference marker, and adjust the reference marker to ensure complete alignment with the lithological interfaces in the borehole images. As shown in Fig. 3(d), the gamma curve of the realigned core closely matches the trend of the logging gamma curve, and the lithology of the core is consistent with that of the borehole images. Thus, the core depth realignment work for well Z104 has been successfully completed.

The borehole image interpretation software Ciflog was used in this study. Ciflog is a logging data processing and interpretation system developed based on advanced computing technologies (Li et al., 2013). Using this software, the fracture orientation at the reference marker below the fragmented interval was determined to be 224°. The horizontal distance between the core reference marker and the marker line is 1.33 cm, and the circumference of the core is 25.21 cm. Using Eq. (1), the orientation of the continuous core below the fragmented segment is calculated to be approximately 205°. Due to the presence of a fragmented segment in the middle of the first-pass core of well Z104, the orientation of the upper continuous core may deviate from that of the lower section. It is necessary to perform further orientation alignment of the upper continuous core. After calculation, the orientation of the upper continuous core is calculated to be approximately 0°. At this point, the core spatial position restoring for well Z104 is complete. Finally, both the core stitching image and the borehole images are oriented with true north, expanding from left to right (Fig. 3(e)). This methodology is applied to all core intervals within the study area.

3.2. Core fracture characteristics

Core observations show that natural fractures are well-developed in the reservoir of the study area (Fig. (4)), with high-angle and vertical shear fractures (45–90°) being predominant, and occasional tensile fractures are observed (Figs. 4(a)–(b) and 5(a)–(b)). Shear fractures exhibit smooth, straight fracture surfaces, often accompanied by striations and steps. The fractures frequently develop as trans-lithological features when they intersect lithological interfaces (Fig. 4(a)–(c)). Tensile fractures have shorter extensions, with curved and undulating fracture surfaces that often terminate at lithological interfaces (Figs. 4(c)–(e) and 5(c)). The sedimentary environment of the study area is characterized by an arid to semi-arid paleoclimate, with alkaline sedimentary waters. The fracture fillings are predominantly gypsum salts, with 49% of the fractures remaining unfilled (Figs. 4(c) and 5(d)). The fracture apertures generally range below 0.2 mm, with only a few tensile fractures showing larger apertures (Figs. 4(c) and (d) and 5(e)). Fifty-five percent of the fractures penetrate through the core, while 45% of the associated smaller-scale fractures do not extend through the borehole (Figs. 4(g) and 5(f)). Fig. 4(h) shows that some fractures develop within the interlayers, with the fractures terminating at the stratigraphic interfaces above and below.

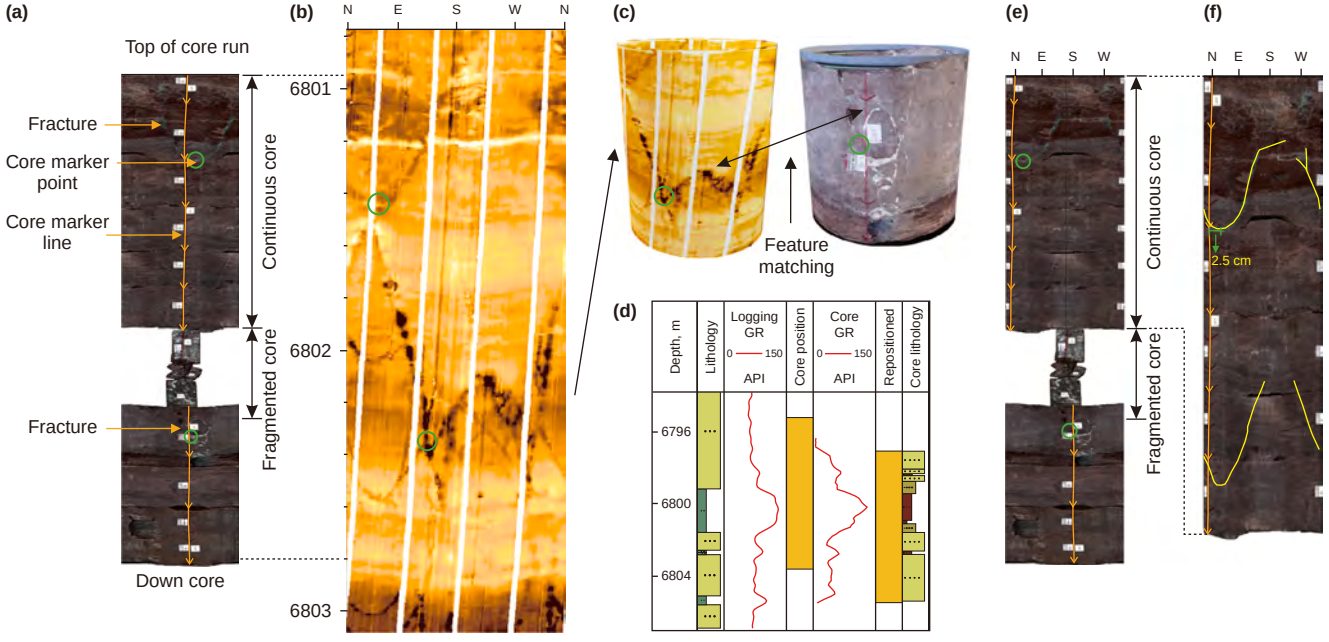

Fig. 3. First-run core spatial realignment workflow in Z104 well. **(a)** Core scanning image stitching. **(b)** Borehole images matched to the depth interval of the core. **(c)** Comparative of fracture features between the core and borehole images. **(d)** Verification of core depth realignment using core-scanned GR data. (**e**) Core stitching after spatial realignment. **(f)** Enlargement of upper features in the first-run fragmented segment of Z104 well.

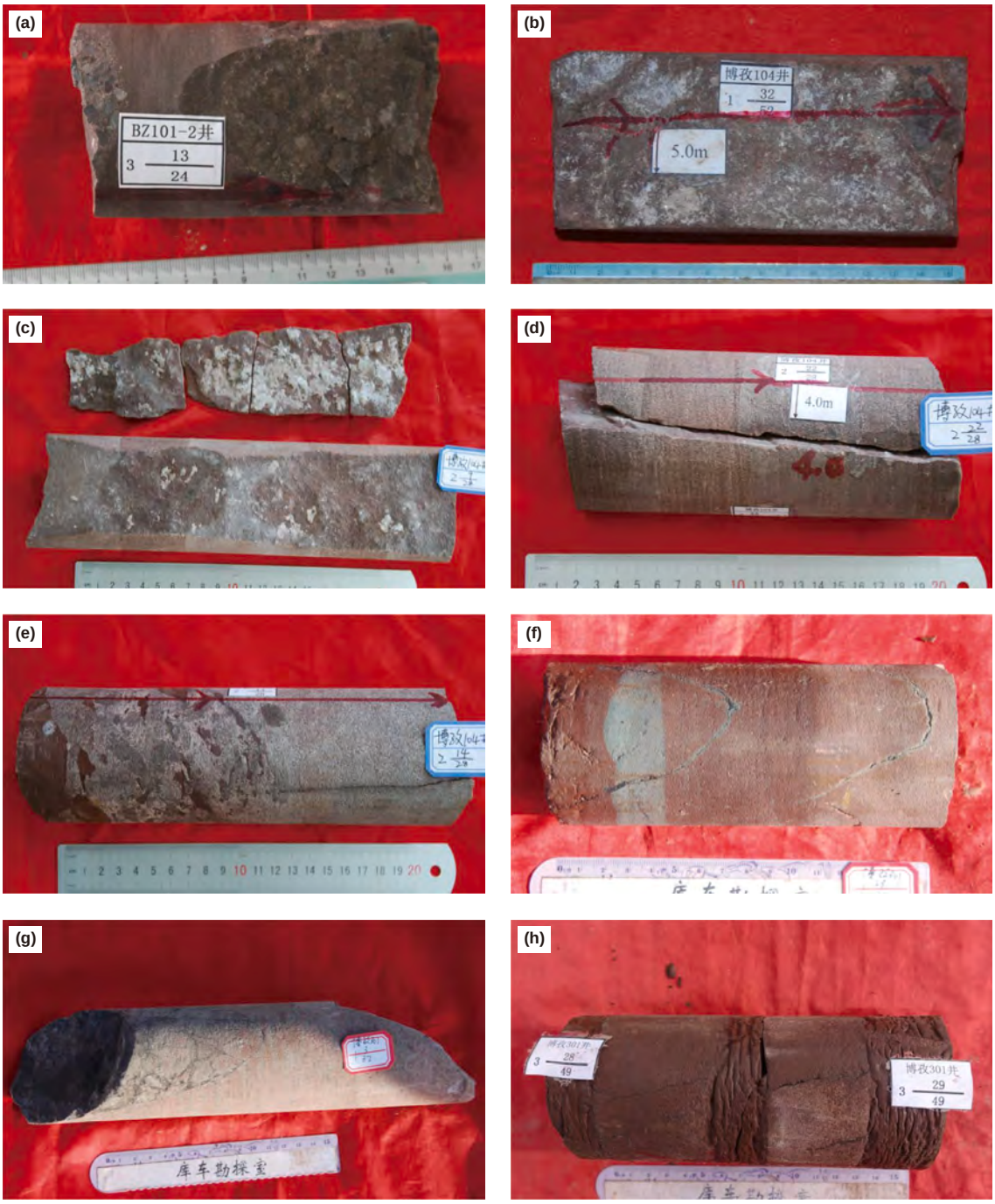

Fig. 4. Photographs of core fracture features. **(a)** Well Z101–2, K_1bx, 7077.42 m, high-angle unfilled shear fracture. **(b)** Well Z104, K_1bs, 6802.42 m, vertical semi-filled shear fracture. **(c)** Well Z104, K_1bs, 6849.01 m, vertical semi-filled tensile fracture. **(d)** Well Z104, K_1bs, 6846.58 m, vertical unfilled tensile fracture. **(e)** Well Z104, K_1bs, 6847.51 m, vertical unfilled tensile fracture terminating against mud breccia. **(f)** Well Z301, K_1bx, 6802.50 m, high-angle shear fracture terminating within a stratigraphic layer. **(g)** Well Z301, K_1bx, 5835.67 m, large-scale fracture with associated small-scale fractures. **(h)** Well Z301, K1bx, 5849.93 m, fractures developed within interlayers.

It is known that the orientation of the reference line in Fig. 3(f) is 0°, and the troughs of the two fracture arcs are approximately 2.5 cm from the marker line. Using Eq. (1), the dips of both fractures on this core interval are back-calculated to be approximately 36°. This method is then applied to calculate the fracture dips for all core samples in the study area.

3.3. Classification of image feature patterns in borehole images

The borehole images feature patterns in the study area are classified into non-linear and linear patterns based on the color combination characteristics, morphological features, sinusoidal curve detection capability, and geological significant. Non-linear patterns can be further subdivided into six categories: massive, band, speckled, graded, chaotic, and anomalous patterns (Fig. 6). Line patterns can be further subdivided into three categories: chord curve, symmetric line, and symmetric shadow line (Fig. 7). Among these, chord curve and symmetric line patterns reflect the features of natural fractures, bedding planes, and hydraulically induced fractures, whereas symmetric shadow-line patterns reflect features of borehole breakout.

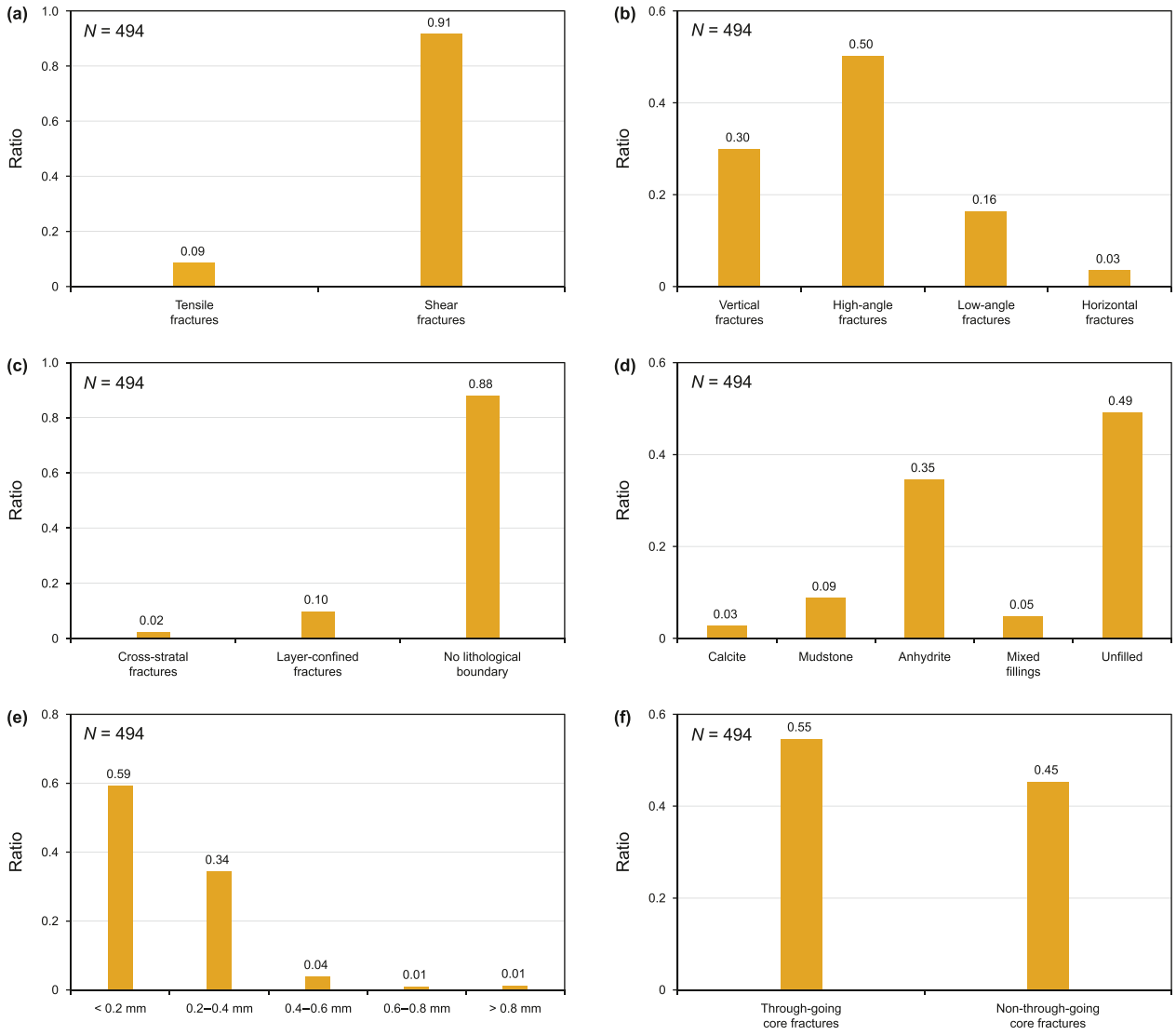

Fig. 5. Statistical charts of core fracture characteristics. **(a)** Mechanical property statistics of core fractures. **(b)** Fracture dip-angle statistics of core fractures. **(c)** Cross-layer extension statistics of core fractures. **(d)** Filling-material statistics of core fractures. **(e)** Aperture statistics of core fractures. **(f)** Scale statistics of core fractures.

3.4. Bidirectional comparison results

Fig. 8 illustrates the process of bidirectional comparing natural fractures in cores with fracture image features manifested as line patterns in borehole images. During this comparison, we found that symmetric lines pattern is actually part of chord curve pattern. Partial chord curve pattern indicates incomplete curves with one flank missing. In contrast, symmetric line pattern arises from the loss of both flanks of the chord curve, leaving only the central segment, which manifests as symmetric lines. When fractures develop within interlayers (Fig. 4(h)) and are constrained above and below, their image features manifest as chord curve patterns with both upper and lower missing, corresponding to symmetric lines. Under certain circumstances, when vertical natural fractures do not penetrate the core (Fig. 8(g)), the paired vertical-line normally seen in images appear as a single line on one side only.

Numerous small-scale core fractures fail to manifest discernible image features in borehole images. As illustrated in Fig. 8(a), several short, narrow fractures are visible in the lower-left corner of the core, yet the corresponding lower-left region of the borehole images shows no matching fracture features. In oil-based mud wells, the fracture image features of cores typically exhibit weak signatures in borehole images. As illustrated in Fig. 8(e) and (f), these fracture image features appear blurred or may even be completely absent.

A statistical analysis was conducted to compare core natural fractures with their corresponding image features in line patterns. As summarized in Table 1, in the Bashijiqike–Baxigai tight-sandstone reservoirs of the Bozi–Dabei area, we estimate that approximately 24% of core-observed fractures display distinct linear-pattern features on borehole images. Within this dataset, wells drilled with water-based mud show a higher correspondence at approximately 44%, whereas oil-based-mud wells show approximately 10%. Further statistical analysis within water-based mud wells shows: tensile, core-penetrating, unfilled, and >0.2 mm fractures exhibit higher image response rates than shear, non-penetrating, filled, and narrower fractures, respectively. Comparison of response rates for the remaining characteristics indicates minimal differences.

Because borehole images quality is poor in oil-based mud, reverse comparison of image features with natural fractures holds

Image feature patterns		Morphology	Borehole images	Core roll-out scan	Geological significance
Massive > 10 cm	Bright				High resistivity formations (e.g., tight sandstone).
	Dark				Low resistivity formations (e.g., mudstone).
	Truncated				Indicators of lithological abrupt changes.
Band > 10 cm	Dark		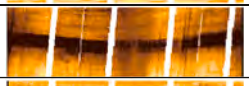		Low-resistivity lithological strata.
	Bright				High-resistivity lithological strata.
	Alternated		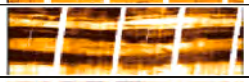		High-resistivity interbedded with low-resistivity strata.
Speckled	Dark		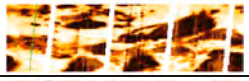		Low-resistivity mud clasts and concretions within relatively high-resistivity strata.
	Bright		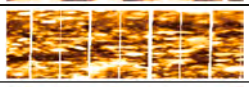		High-resistivity gravels and calcareous within relatively low-resistivity strata.
Graded	Gradual color gradation				Color gradation changes from light to dark indicates progressive grain size variation.
Chaotic	Distortion folding				Deformed bedding, convolute bedding, and other soft sediment deformation structures.
Anomalous	Blank	⁄		⁄	Without geological significance, representing operational anomalies during tool initialization and termination phases, abnormal tool movement, and poor pad contact.
	Image distortion	⁄		⁄	
	Regular stripes	⁄		⁄	
	Image blur	⁄		⁄	

Fig. 6. Non-linear pattern classification in borehole images and explanation of corresponding geological significance.

little value. Therefore, a reverse comparison between line pattern image features in borehole images and natural fractures in cores was conducted exclusively in water-based mud wells. The statistical results indicate that (Table 2): ninety-one percent of fracture image features in borehole images can be matched to corresponding core fractures, whereas 9% of fracture images have no corresponding fractures in the cores. These unmatched fracture image features indicate that the fractures, after penetrating the borehole wall, terminate within the gap between the borehole wall and the core. Therefore, these fracture image features have no corresponding fractures in the cores.

3.5. Image response pattern of natural fractures

An image response pattern for natural fractures in ultra-deep tight sandstone boreholes was established, based on a bidirectional comparison between natural fractures and their image features, taking into account dip angle, through-layer connectivity, and spatial position within the borehole. This model was developed under ideal conditions, assuming that all natural fractures reach the detection threshold of borehole images and yield high-quality, undeformed image features.

When natural fractures laterally penetrate the borehole, they simultaneously penetrate both the core and the borehole wall. Fractures of varying dip angles display distinct characteristics in borehole images. (I) Vertical fractures manifest as two vertically symmetric lines image features (Figs. 4(b)–(d) and 9(a)), with their imaged top and bottom depths and orientations consistent with those of the core fractures. (II) Oblique fractures manifest as chord curve image features (Figs. 4(a) and 9(b)); their imaged top and bottom depths exceed those of the core fractures, while their mid-depths and orientations are completely consistent. (III) Horizontal fractures manifest as a nearly horizontal linear image feature (Fig. 9(c)); their imaged top and bottom depths and orientations consistent with those of the core fractures.

Some natural fractures in the study area terminate within stratigraphic layers; the following cases warrant special attention. (I) Vertical fractures penetrate the borehole but not the core. In this case, no fractures are present in the core, yet borehole images still display two vertically symmetric lines image features (Fig. 9(d)). (II) Vertical natural fractures terminate within the

Image feature patterns		Morphology	Borehole images	Core roll-out scan	Geological significance
Chord curve	Bright				Representing geological features that cut the borehole, such as faults, fractures, and bedding planes. The color is determined by the resistivity of the filling material.
	Dark		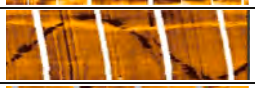		
	Partial				Representing geological features terminate within the borehole.
Symmetrical lines	Vertical				Representing vertical fractures or fracture-induced fractures.
	Inclined				Representing hydraulically induced fractures or fractures developed within interlayers.
					
Symmetrical shadow lines	Vertical				Representing borehole breakout.
	Inclined				

Fig. 7. Linear pattern classification in borehole images and explanation of corresponding geological significance.

borehole, penetrating the borehole wall on only one side. Under these conditions, the core may exhibit one of three cases: (a) a vertical fracture fully penetrates the core (Fig. 9(e)); (b) a vertical fracture penetrates only one side of the core (Fig. 9(f)); or (c) no fractures are present in the core (Fig. 9(g)). In all cases, borehole images display a single vertical line image feature. (III) Oblique fractures terminate within the borehole, penetrating the borehole wall on only one side. Under these conditions, the core may exhibit one of three cases: (a) Oblique fractures fully penetrate the core (Fig. 9(h)); (b) oblique fractures partially penetrate the core (Fig. 9(i)); or (c) no oblique fractures are present in the core (Fig. 9(j)). In all cases, the fractures intersect part of the borehole wall, appearing as partial chord curve image features in borehole images. In cases (a) and (b), the imaged termination depths of these features correspond exactly to those of the core fractures.

Natural fractures in the study area exhibit poor through-layer connectivity (Ju et al., 2025), with most fractures terminating at lithological interfaces (Fig. 5(c)). The following cases warrant special attention. (I) When vertical fractures penetrate both the borehole and the core and are constrained by lithological interfaces within the borehole, they still manifest as two symmetric lines image features (Fig. 9(i) and (k)). (II) Vertical fractures penetrate the borehole but not the core and terminate at lithological interfaces; this case is analogous to the patterns shown in Fig. 9(d)–(g). (III) The case of oblique fractures terminating at lithological interfaces is more complex. When oblique fractures penetrate the borehole and are constrained by lithological interfaces within it, two distinct case s may arise: (a) Oblique fractures penetrate the borehole on one side and terminate at a lithological interface (Fig. 9(m)). This case, similar to the patterns shown in Fig. 9(h)–(j), manifests as partial chord curve image features in borehole images, indicating that the fracture termination corresponds to a layer interface. (b) Oblique fractures terminate at lithological interfaces on both sides; in this case, evaluation requires reference to interlayer thickness and fracture dip angle.

Several key parameters are introduced here. As shown in Fig. 10(a), the left side indicates the interlayer thickness, while the right side marks the amplitude of the chord curve. In Fig. 10(b), the black dot on the right represents the center of the fracture plane; the central black dot indicates the projected position of the fracture center after horizontal displacement to the borehole center. The blue line connecting the two points denotes the horizontal offset between the fracture center and the borehole center. (i) When the interlayer thickness is less than the amplitude of the chord curve, partial chord curve image features manifest in borehole images. (ii) When the horizontal offset distance of the fracture-plane center from the borehole center is less than $\frac{H}{2\tan\alpha}$, partial chord curve image features manifest in borehole images (Figs. 9(n) and 10(a)). When interlayer thickness exceeds the amplitude of the chord curve, further differentiation is required. (iii) When the horizontal offset distance of the fracture-plane center from the borehole center lies between $\frac{H}{2\tan\alpha}$ and $R-\frac{\tan\alpha}{2H}$, partial chord curve image features manifest in borehole images (Figs. 9(o) and 10(b)). In both cases (ii) and (iii), the image features correspond exactly to those of the core fractures in terms of termination depth. (iv) When the horizontal offset distance exceeds $R-\frac{\tan\alpha}{2H}$, the fracture pattern transitions to that shown in Fig. 9(m), manifesting partial chord curve image features in borehole images.

$$\begin{cases} R\tan\alpha \le H \\ R\tan\alpha > H, \begin{cases} X \le \dfrac{H}{2\tan\alpha} \\ \dfrac{H}{2\tan\alpha} < X < R-\dfrac{\tan\alpha}{2H} \\ R-\dfrac{\tan\alpha}{2H} \le X \end{cases} \end{cases} \tag{2}$$

where H is the interlayer thickness, m; α is the fracture dip angle, °; R is the borehole radius, m; $R\tan\alpha$ is the chord curve amplitude (dimensionless); $\frac{H}{2\tan\alpha}$ is the horizontal offset distance of the fracture-plane center from the borehole center, m; and $R-\frac{\tan\alpha}{2H}$ is

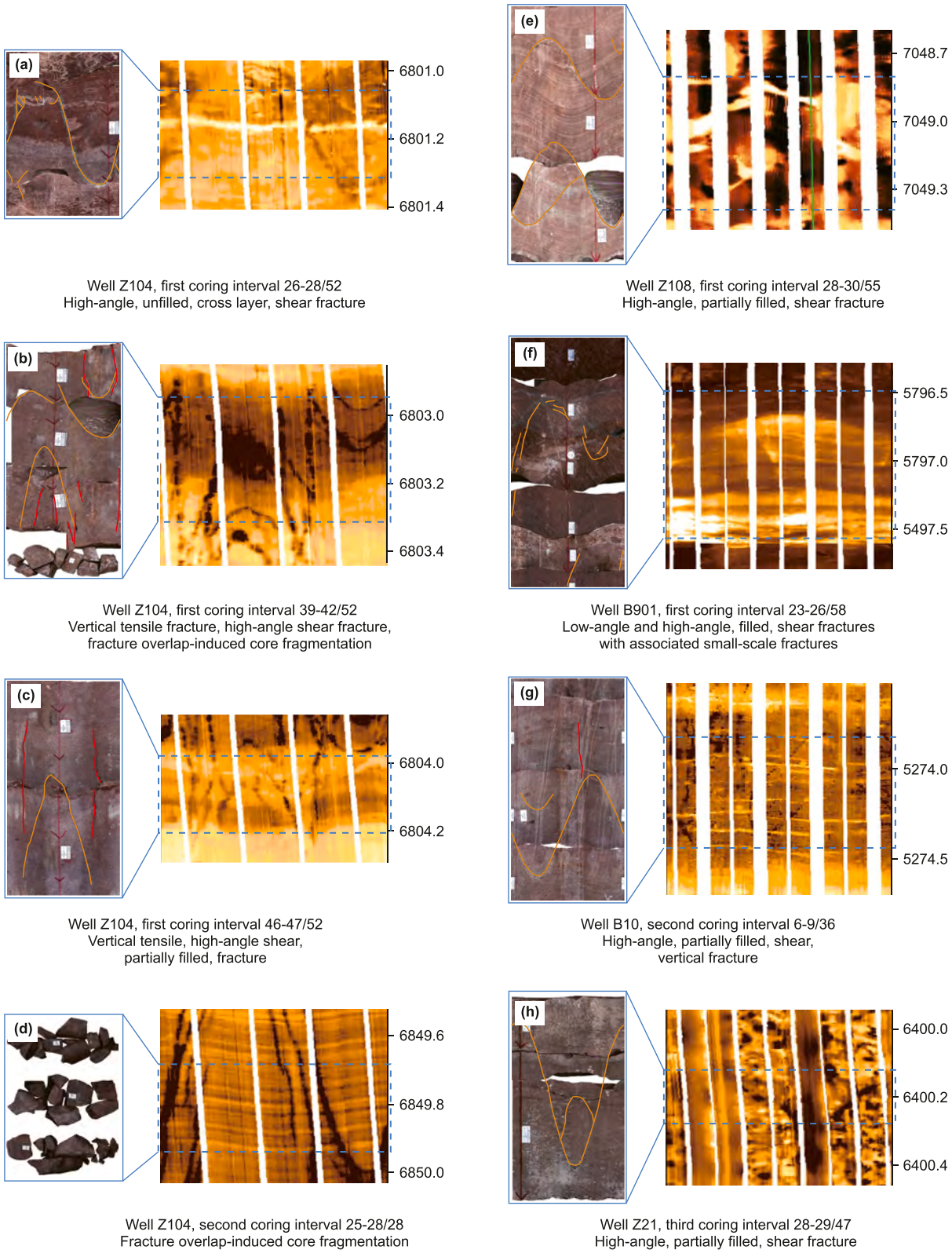

Fig. 8. Comparison of core fracture and their corresponding borehole images response features.

the maximum horizontal offset distance of the fracture-plane center from the borehole center, m.

In real borehole images, the chord curve image features of fractures seldom begin at zero phase; their initial phase shifts according to the relative alignment between the fracture location and the tool button distribution. Moreover, fracture image features are not uniformly dark and must be interpreted in conjunction with fill-material properties and the mud system. Multiple

Table 1
Count of core natural fractures exhibiting images features in borehole images.

Fracture type	Water-based mud				Oil-based mud			
	Core fractures	Responsive	Non-responsive	Response ratio, %	Core fractures	Responsive	Non-responsive	Response ratio, %
Tensile	22	14	8	64	24	8	16	33
Shear	178	74	104	42	270	20	250	7
Penetrating the core	130	73	57	56	143	16	127	11
Not penetrating the core	70	15	55	21	151	12	139	8
Filled	113	38	75	34	139	8	131	6
Unfilled	87	50	37	57	155	20	135	13
Vertical	70	33	37	47	81	12	69	15
High-angle	105	47	58	45	144	9	135	6
Low-angle	23	7	16	30	57	5	52	9
Horizontal	2	1	1	50	14	2	12	14
Aperture >0.2 mm	114	57	57	50	114	15	99	13
Aperture <0.2 mm	86	31	55	36	180	13	167	7
Cross-layer	9	4	5	44	14	3	11	21
Non-cross-layer	25	8	17	32	11	1	10	9
Total	200	88	112	44	294	28	266	10

Table 2
Count of fracture image features corresponding to core fractures.

Image features type	Water-based mud			
	Image features	Corresponding core fractures	Non-corresponding core fractures	Correspondence ratio, %
Complete chord curve	122	122	0	100
Partial chord curve	30	26	4	87
Symmetrical Vertical line	20	14	6	70
Single vertical line	24	18	6	75
Symmetrical Inclined line	4	2	2	50
Total	200	182	18	91

response modes often overlap, and different fracture signals should be carefully separated and identified by comparing image-feature morphology, grayscale variations, and spatial distributions.

3.6. Application performance of the pattern in fracture identification

We applied the fracture image response pattern established in this study to identify fractures in key wells in the study area (Figs. 11–14). We compared the fracture identification results from our borehole images with those from Schlumberger, CNPC Logging, and other service providers (Tables 3 and 4). The statistical results indicate that fracture identification rates in water-based and oil-based mud increased by 17% and 3%, respectively. Notably, in wells with superior imaging quality, response patterns associated with incomplete chord curves or fractures developing within interlayers exhibited higher identification improvement rates (Fig. 9(d)–(o)).

4. Discussion

4.1. Analysis of bidirectional comparison results

In the Bashijiqike–Baxigai tight-sandstone reservoirs of the Bozi–Dabei area, numerous small-scale fractures (with narrow apertures) fall below the detection limits of borehole-imaging tools. In addition, tool sticking, rotational instability, and associated artifacts (blank sectors, speckling, and striping) compromise the faithful expression of fracture signatures on borehole images (Lai et al., 2024b). Under these constraints, in this study area and following our strict matching criteria, we estimate that only about 24% of core-observed fractures display distinct linear-pattern features on borehole images.

Oil-based drilling fluids significantly reduce borehole fluid conductivity, severely impacting logging methods that rely on fluid conductivity. In oil-based mud environments, borehole resistivity increases and the resistivity contrast between the oil-based drilling fluid in fractures and the rock matrix is minimal. Consequently, micro-resistivity imaging quality is poor, making fracture identification challenging (Tang et al., 2017). By contrast, water-based mud, owing to its higher conductivity, lowers borehole fluid resistivity, thereby facilitating clearer differentiation between fracture fluids and the rock matrix in micro-resistivity imaging. Consequently, in water-based mud environments, borehole imaging achieves significantly higher fracture identification resolution and accuracy compared to oil-based mud conditions.

Comparison of response rates for various core fracture characteristics in water-based mud wells reveals that: within the borehole, fractures with larger scales and higher efficacy account for a greater proportion of responses in borehole images. When fractures are small in scale, they may go undetected due to falling below the instrument's resolution threshold. And their image often appears too narrow and fragmented to qualify as identifiable image features. Fracture image coloration depends on the resistivity contrast between the fracture fluid or fill material and the surrounding rock matrix (Wang, 2023). As fracture efficacy increases, greater volumes of low-resistivity mud invade the fracture pathways. Target-zone sandstone, silty mudstone, and muddy siltstone host rocks exhibit resistivities that are relatively higher than that of the low-resistivity mud. Consequently, the dark response images in borehole images form a stark contrast against the high-resistivity surrounding rock. By contrast, low-efficacy fractures often have narrow apertures and are filled

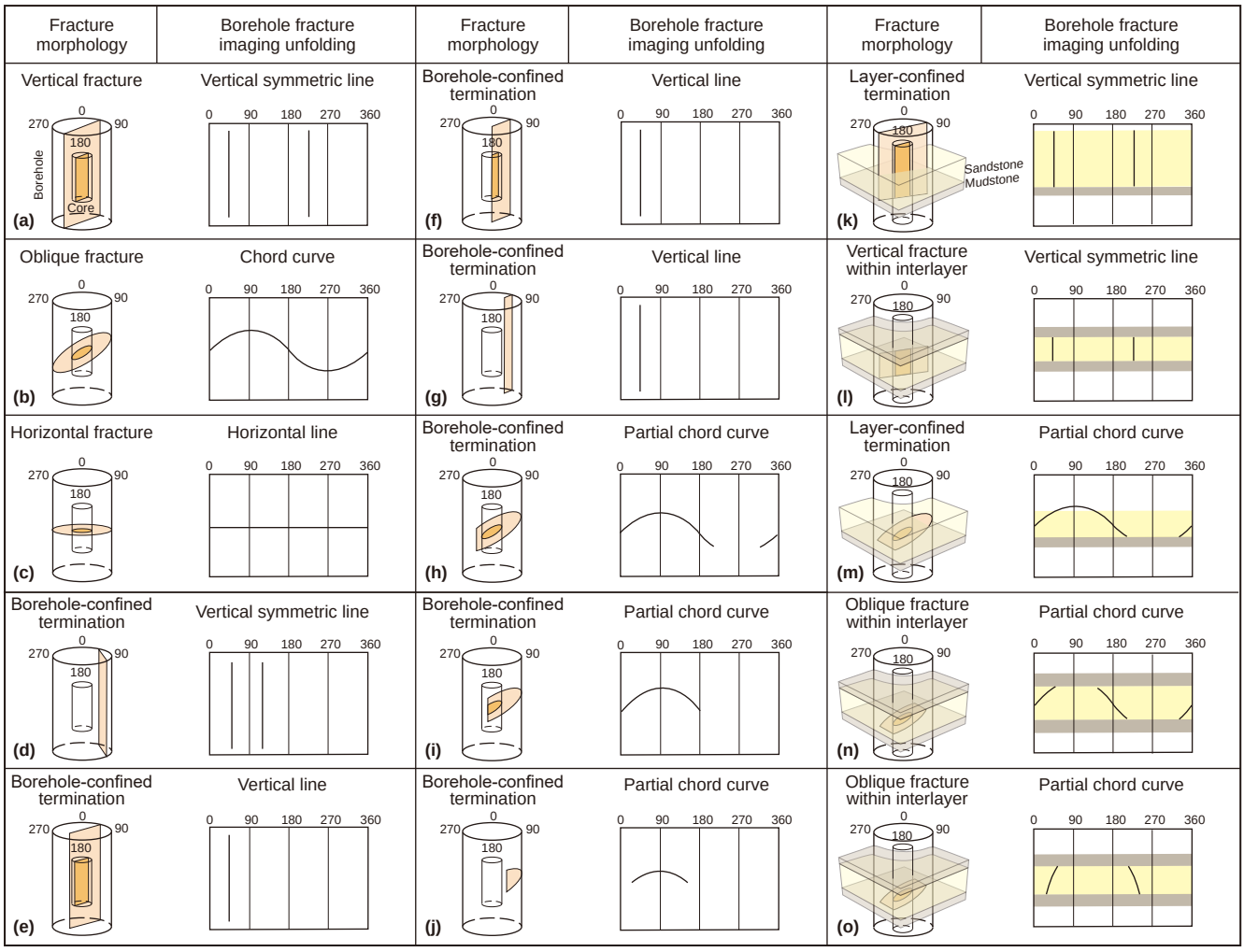

Note: In the figure, the complete or partial sinusoidal curve features of natural fractures are represented as sine curves, with the initial phase set to 0.

Fig. 9. Image response pattern of natural fractures in borehole images.

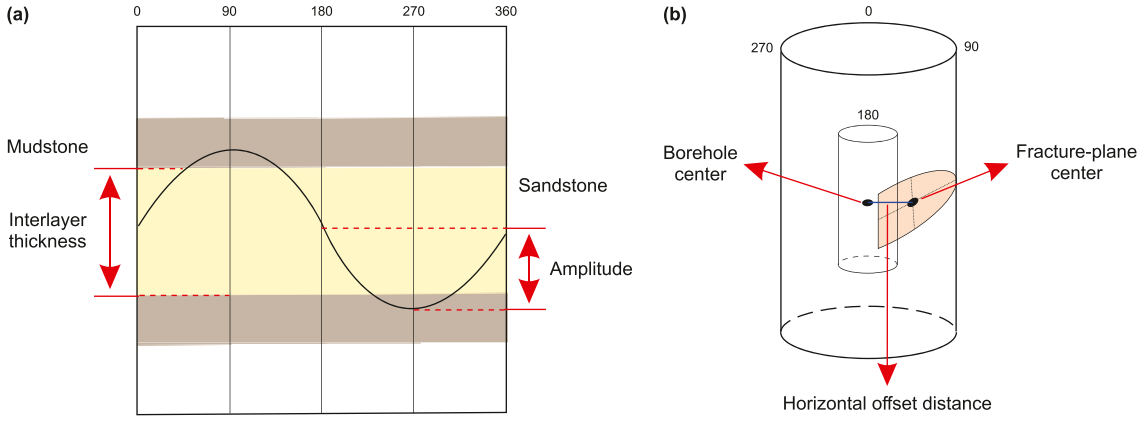

Fig. 10. Description of spatial parameters of natural fractures within the borehole. **(a)** Schematic illustration of interlayer thickness and amplitude of the chord curve. **(b)** Schematic illustration of the fracture plane center, borehole center, and their horizontal offset.

with high-resistivity materials such as residual calcite or quartz. These fractures produce bright responses that closely match the surrounding rock resistivity. Consequently, they lack distinct fracture image features in borehole images and cannot be reliably identified.

Additionally, the bidirectional comparison process may be confounded by other factors. As illustrated in Fig. 8(h), the image features of natural fractures are obscured by two vertically distributed shadows, making it difficult to compare the two data sources.

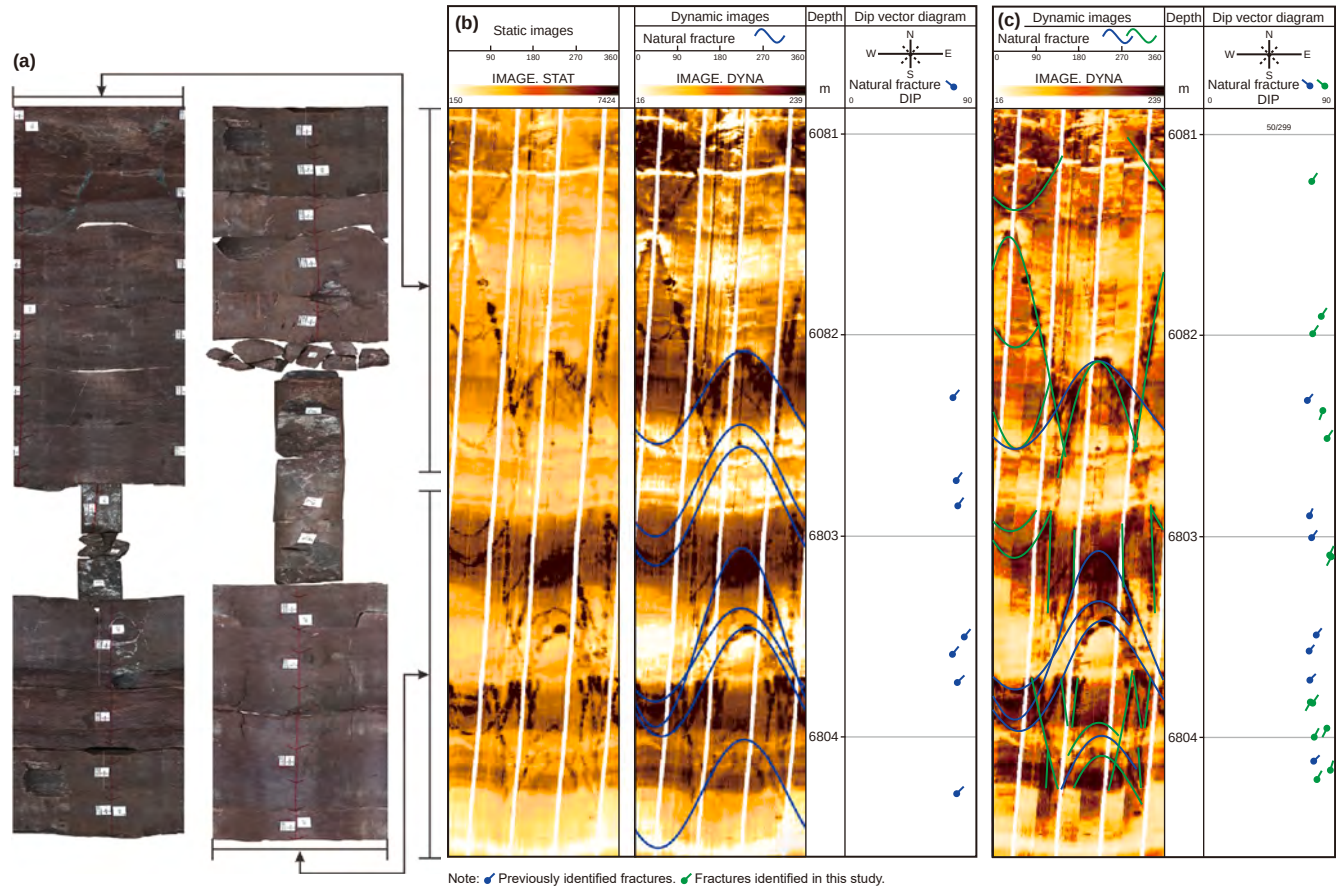

Fig. 11. Comparison of borehole images fracture identification results in Well Z104 between previous work and the image response pattern. **(a)** Stitched core images. **(b)** Previous identification results. **(c)** Image response pattern results.

4.2. Challenges in fracture identification using borehole images

Applying the imaging response pattern established in this study improves fracture detection rates in borehole images. However, other factors still introduce discrepancies in the identified features and counts of core fractures (Tables 1 and 2). Moreover, these factors can sometimes render fractures entirely unrecognizable.

Operators performing fracture identification should carefully consider and minimize all sources of interference. Cross-validation across multiple datasets should be employed to enhance the accuracy of extracting fracture image features and prevent identification errors or misinterpretations.

4.2.1. Core fractures exhibit no image features

The patterns shown in Fig. 9(d)–(g) and (j) occur when no fractures are present in the core, yet the borehole images continue to display fracture image features. During core retrieval and handling, changes in external conditions can cause fractures that were tightly closed under in situ high-pressure conditions to open significantly (Pan et al., 2024). Artificial fractures resembling natural ones may also develop during this process (Wu et al., 2007; Qin et al., 2025). Although the apertures of these fractures exceed the detection threshold, their corresponding image features do not manifest in borehole images.

4.2.2. Inconsistent feature recognition between core and borehole images

Due to heterogeneities in the regional stress field, lithological variations, fluid flow dynamics, and multiple tectonic episodes, fractures may have undergone repeated cycles of opening, closure, and infill (Pan et al., 2024; Hu et al., 2025). In half-filled fractures, the unfilled sections are still invaded by drilling mud, producing intermittent chord curve image features in borehole images (Yang et al., 2008). In contrast, the features displayed on the core represent only a localized segment. As illustrated in Figs. 3(c) and 15(a), the core indicates a fully filled fracture, whereas the borehole images predominantly show characteristics of a half-filled fracture. Moreover, cores frequently become incomplete or fragmented after multiple retrieval and sampling operations (Wu et al., 2007; Qin et al., 2025), preventing accurate preservation of true fracture features. Consequently, the localized fracture characteristics observed in core samples differ markedly from the macroscopic features identified in borehole images. In oil-based mud environments, both unfilled fractures and fractures filled with high-resistivity materials exhibit bright image features (Lai et al., 2015). The high resistivity of the mud degrades image clarity, making it difficult to distinguish between unfilled and high-resistivity filled fractures. Consequently, this leads to discrepancies in fracture feature identification between core observations and borehole imaging. Oil-based mud may also exhibit oil–water separation under certain conditions (Li, 2017). In such cases, an upper oil layer and a lower water layer form, and the low-resistivity water invades fractures, producing dark image features in borehole images. This phenomenon further exacerbates the difficulty of accurately identifying fracture image features.

4.2.3. Absence and distortion of chord curve image features

In addition to the missing fracture image features in Fig. 9(d)–(g) and (j), other factors can also lead to the absence of

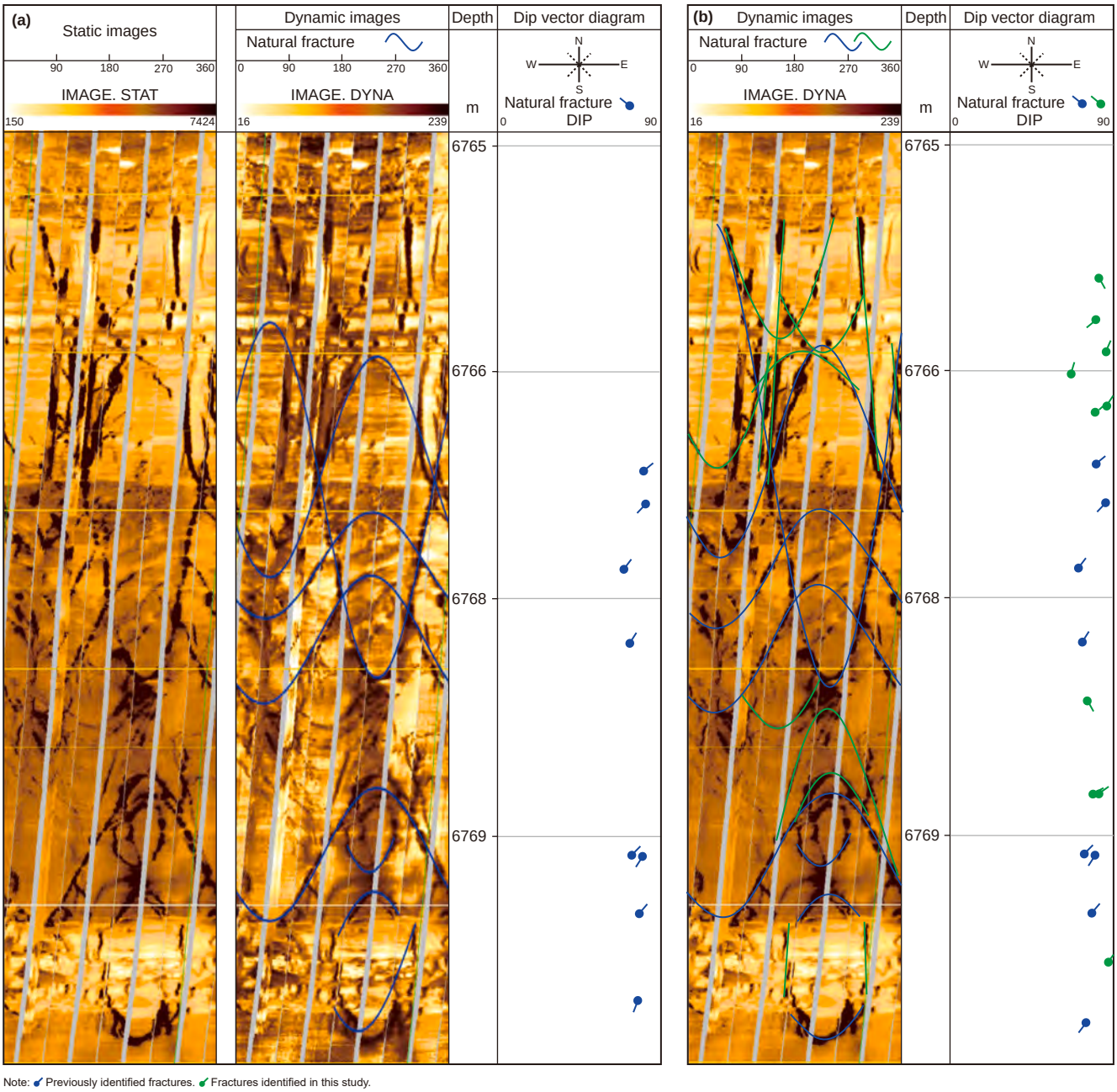

Fig. 12. Comparison of borehole images fracture identification results in Well Z104-1 between previous work and the image response pattern. **(a)** Previous identification results. **(b)** Image response pattern results.

chord curve image features. When natural fractures propagate across layers, the aperture of a given fracture is generally greater in sandstone than in mudstone. Mudstone is typically rich in clay minerals, which impart high plasticity and viscosity, making it more susceptible to plastic deformation under burial pressure and stress concentration. As a result, fractures in mudstone often fail to maintain their original aperture and become partially closed (Chen et al., 2017; Ma et al., 2022). Sandstone possesses a higher elastic modulus as well as greater compressive and tensile strengths (Li et al., 2020a). Consequently, once fractures form, they can better maintain their original aperture. As illustrated in Figs. 8(a) and 15(b), the core shows a natural fracture propagating across layers, with the aperture decreasing within the mudstone. The mudstone interval produces no clear response images in borehole images, resulting in missing chord curve image features.

During drilling operations, borehole wall stability is directly influenced by the combined effects of in-situ stress, drilling fluid density, and borehole pressure. When the in-situ stress on the borehole wall exceeds the failure strength of the surrounding rock, the formation loses its original integrity, resulting in localized or extensive collapse and fracturing of the borehole wall (Sun et al., 2018). Borehole wall collapse typically manifests as irregular geometries and borehole enlargement on caliper logs. This deformation causes originally continuous, regular chord curve image features to appear noticeably distorted or discontinuous in borehole images (Fig. 15(c) and (d)).

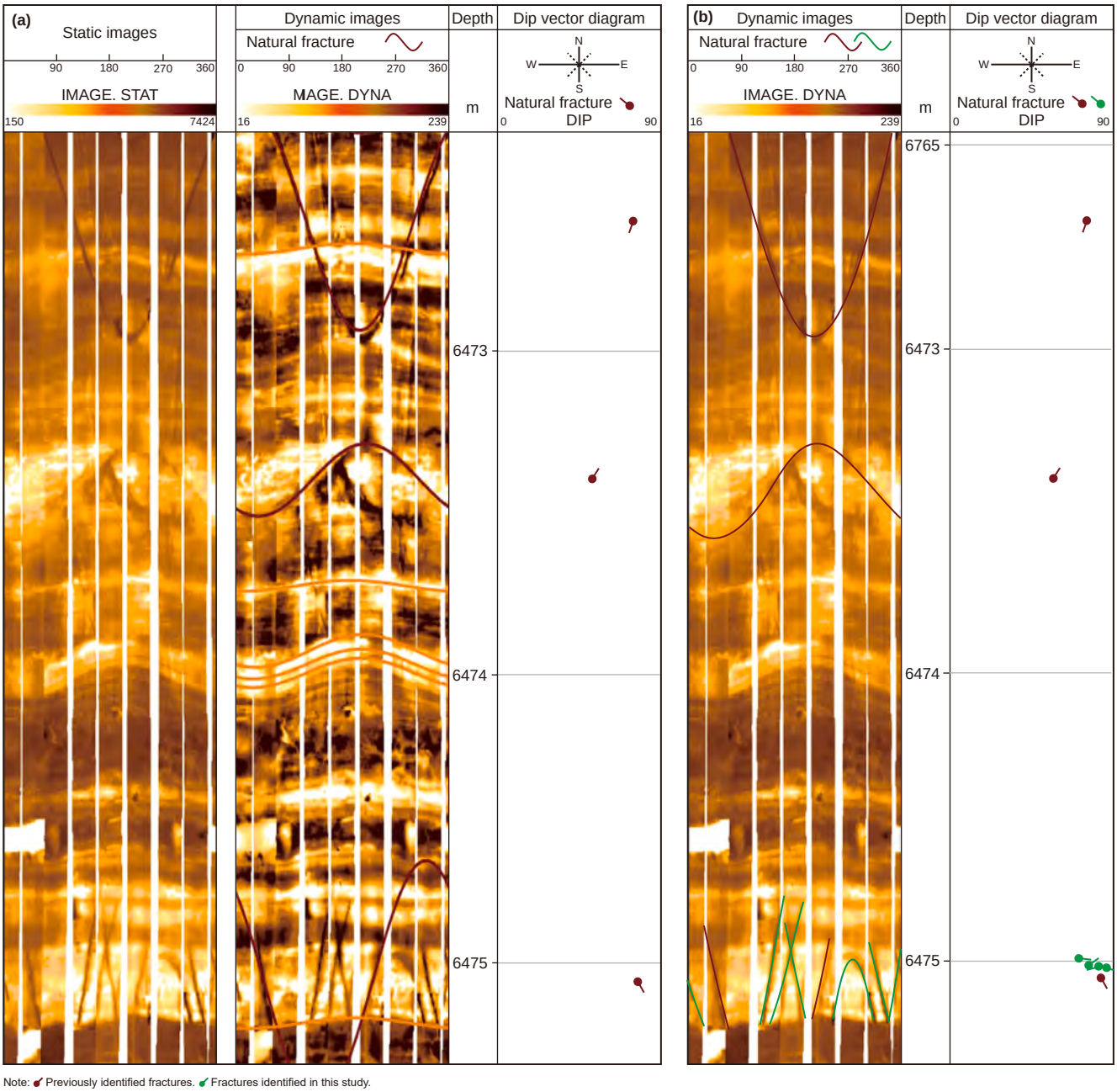

Fig. 13. Comparison of borehole images fracture identification results in Well Z105 between previous work and the image response pattern. **(a)** Previous identification results. **(b)** Image response pattern results.

The presence of filter cake often blocks pore spaces and fractures in the borehole wall, coating the formation and restricting fluid invasion (Su et al., 2024). This blockage prevents the original fill or fluid characteristics within fractures from exhibiting a clear electrical contrast with the surrounding rock (Dong et al., 2023). Coupled with borehole contraction, this effect causes chord curve image features to disappear or become markedly blurred in borehole images.

4.2.4. Inaccurate fracture count identification

Within stratigraphic intervals where natural fractures develop, multiple fractures are often parallel or intersecting, forming mesh-like or even fragmented networks (Ye et al., 2023). Multiple fracture sets crosscut one another with slight offsets, causing the characteristic sinusoidal curves of some fractures to disappear. Instead, these fractures typically appear as a chaotic, discontinuous network of short lineations (Sun, 2016). During fracture identification using borehole images and core, the complex, convoluted image features hinder the reconstruction of fracture chord curves. Consequently, this limitation prevents accurate quantification of the true fracture count (Fig. 15(e)).

Previous studies have shown that when the spacing between two fractures is below approximately 5.00 mm, imaging-log features cannot distinguish them separately, manifesting as a single chord curve (Ke, 2008). Consequently, this limitation leads to an underestimation of the true fracture count during identification.

4.2.5. Fracture identification errors

In borehole images, the image features of natural fractures closely resemble those of induced fractures, borehole breakouts,

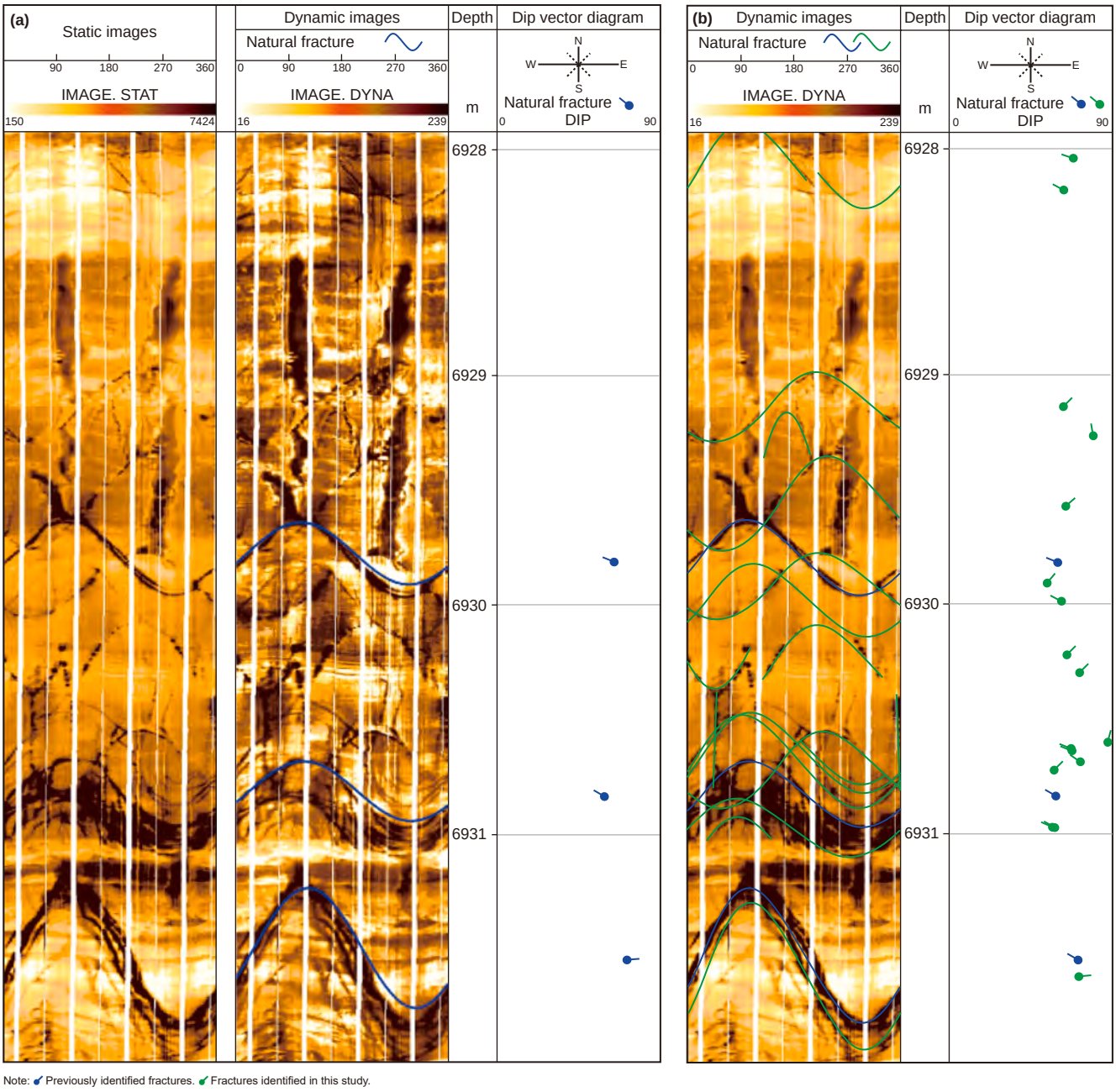

Fig. 14. Comparison of borehole images fracture identification results in Well Z1701 between previous work and the image response pattern. **(a)** Previous identification results. **(b)** Image response pattern results.

Table 3
Improvement in natural fracture identification rate using the image response pattern in water-based mud wells.

Well name	Core run	Depth interval, m	Core fractures	Previous identification rate, %	Image response pattern identification rate, %	Improvement, %
Z104	First	6797.00–6805.41	36	33	20	33
	Second	6845.13–6849.88	8	25	7	25
Z24	First	7217.96–7230.56	16	13	6	13
Z102	First	6755.87–6762.63	18	0	8	0
	Second	6764.07–6771.57	15	20	8	20
	Third	6771.57–6780.07	10	0	2	0
	Fourth	6779.97–6787.73	2	0	0	0
	Fifth	6854.70–6866.58	10	10	2	10
Z2402	First	7204.75–7213.55	5	40	3	40
Z106	First	6796.70–6803.70	19	11	2	11
Total			139	34	58	17

Table 4
Improvement in natural fracture identification rate using the image response pattern in oil-based mud wells.

Well name	Core run	Depth interval, m	Core fractures	Previous identification rate, %	Image response pattern identification rate, %	Improvement, %
Z301	First	5838.47–5843.59	31	9	12	10
	Second	5843.59–5847.53	17	4	4	0
	Third	5847.53–5855.81	45	6	8	4
	Fourth	5855.81–5864.06	60	5	6	12
	Fifth	5878.10–5886.66	12	3	5	17
	Sixth	5931.15–5934.10	10	3	3	0
B12	First	5394.00–5402.54	102	4	7	3
	Second	5440.50–5448.60	13	3	3	0
	Third	5448.77–5456.92	27	4	4	0
B12-8	First	5888.67–5892.82	10	1	1	0
Total			327	42	53	3

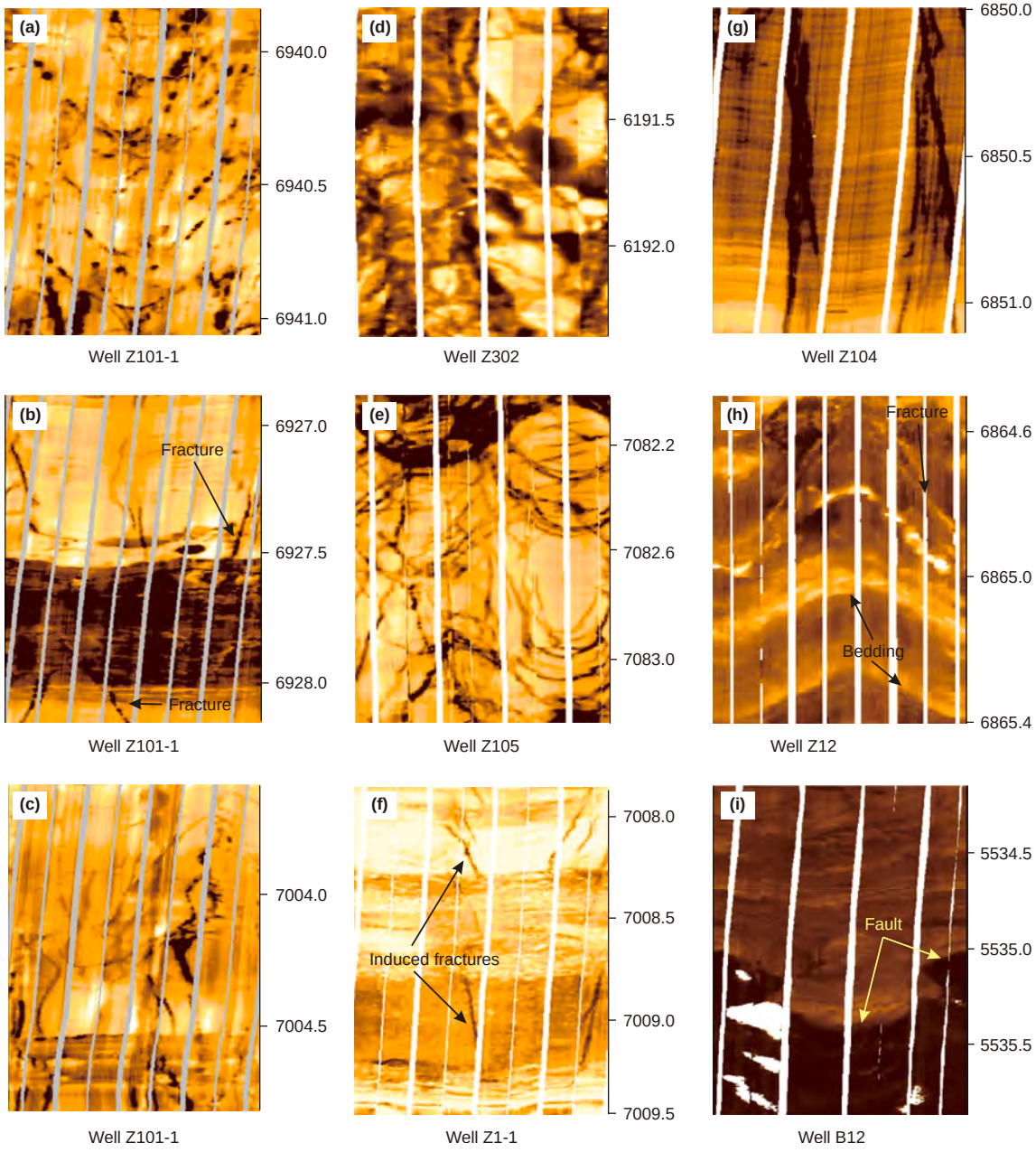

Fig. 15. Summary of commonly misidentified borehole image features in fracture interpretation.

bedding planes, lithological interfaces, bands, and minor faults, often resulting in misidentification. Therefore, accurately distinguishing natural fractures from these similar features is essential for enhancing fracture identification accuracy.

The following summarizes the morphological and characteristic differences between oblique natural fractures and induced fractures: (I) Induced fractures form instantaneously under external stress and their development is governed solely by in-situ stress. Consequently, they exhibit orderly alignment, high regularity, and image features with 180° symmetry. In contrast, natural fractures form through multiple tectonic episodes and are subsequently modified by groundwater dissolution and mineral precipitation, resulting in their irregular development. (II) Induced fractures typically align parallel to the borehole axis, terminate at soft formation interfaces, and lack significant infill, appearing as low-resistivity features. As these fractures often do not fully penetrate the borehole, they fail to generate the characteristic sinusoidal chord curves in borehole images (Li et al., 2005) (Fig. 15(f)). In contrast, natural fractures may fully penetrate the borehole and display irregular fracture surfaces with substantial variations in aperture. (III) Induced fractures typically exhibit limited propagation, align predominantly parallel to the maximum principal stress direction, and frequently occur as clustered sets within the same borehole interval.

Borehole breakouts typically produce an elliptical borehole cross-section oriented perpendicular to the current maximum horizontal principal stress. Over a consistent interval, they manifest as two broad, dark, linear bands symmetrically disposed at 180°. Within these dark zones, geological features are indistinct and boundaries blurred (Cao et al., 2022), often leading to confusion with vertical natural fractures (Fig. 15(g)).

Bedding planes, lithological interfaces, and muddy streaks form during sedimentary deposition and generally conform to the bedding orientation without cutting across strata. Among these, bedding planes typically appear as parallel or subparallel sets, exhibiting regular image features. Muddy streaks on electrical imaging logs present as broad, regular dark bands. These bands typically run parallel to bedding planes and exhibit relatively sharp boundaries. Muddy streaks or mud-filled fractures invariably exhibit elevated natural gamma readings and reduced resistivity. Therefore, by leveraging conventional logging curves, these features can be effectively differentiated (Lai et al., 2015, 2022a, 2024a, 2024b). Notably, bedding planes and natural fractures are prone to misclassification in high-deviation wells (Fig. 15(h)).

Minor faults arise from tectonic movements that displace strata, characterized by discontinuous or offset bedding, and manifest in imaging logs as abrupt bright–dark truncations (Su et al., 2025) (Fig. 15(i)). In contrast, natural fractures primarily reflect rock breakage without appreciable displacement.

4.2.6. Comparison of fracture under different mud environments

Comparative studies of fracture characteristics and development patterns across different wells must be conducted under identical mud systems and logging tool conditions. Without such standardization, any conclusions drawn are entirely unreliable (Liu et al., 2023). Failure to standardize the mud system and logging tool conditions may introduce systematic errors in fracture characterization. Such inconsistencies can result in underestimation or overestimation of fracture density, as well as misclassification of fracture types. These issues not only compromise the reliability of inter-well comparisons but may also misguide reservoir evaluation and development strategies. We therefore emphasize the necessity of conducting inter-well comparative studies under controlled conditions to ensure data comparability and interpretational accuracy.

4.3. Future development directions

Currently, fracture identification via borehole images relies primarily on two-dimensional planar images of the borehole wall unfolded over 360°. However, this approach has limitations when dealing with fractures exhibiting complex three-dimensional geometries or incomplete chord curves. Extending borehole images analysis into three-dimensional space for fracture detection would offer a more intuitive visualization of core fracture propagation toward the borehole wall. This will improve our understanding of the spatial morphology of fractures lacking chord curves image features and clarifies their cutting relationships with the borehole wall. Building on this, three-dimensional fracture identification overcomes image distortions induced by borehole diameter variations (Dong et al., 2023). This approach markedly reduces the risk of fracture misclassification or omission caused by borehole irregularities.

We supplemented the detection of fractures exhibiting incomplete chord curve image features. We also targeted fractures that developed within interbeds for additional identification. Building on the findings of this study, we supplemented the detection of fractures exhibiting incomplete chord curve image features and those developing within interlayers for additional identification. We propose that these fractures should be incorporated into the existing fracture characterization framework in future studies. The system delineates the orientation, extension, and structural effectiveness of each fracture type. By integrating geological context, it also clarifies the genetic mechanisms and temporal sequences underlying different fracture origins. These enhancements improve the accuracy of fracture genesis interpretation and spatial distribution prediction. Moreover, this framework supports the evaluation of fracture-related contributions to reservoir connectivity, permeability enhancement, and productivity enrichment—particularly in tight and heterogeneous reservoirs. Such integration would enhance the comprehensive evaluation of fracture networks and their roles within the reservoir.

Current machine-learning approaches for fracture detection in borehole images rely predominantly on intact chord curve image features to infer the presence of fractures. These patterns fail to consider scenarios in which chord curve are incomplete or vertical fractures manifest as two symmetric lines. Therefore, new feature-extraction metrics must be introduced into existing algorithmic frameworks. Through these improvements, the automated detection system can accurately identify fractures with incomplete chord curves. It can also detect fractures that manifest as two symmetric lines. Thereby, enhances the overall accuracy and reliability of fracture identification.

5. Conclusion

In this study, we established an image response pattern for natural fractures in borehole images. The conclusions are as follows:

In the Bashijiqike–Baxigai tight-sandstone reservoirs of the Bozi–Dabei area, we estimate that approximately 24% of core-observed fractures display distinct linear-pattern features on borehole images. Within this dataset, approximately 44% in water-based-mud wells and approximately 10% in oil-based-mud wells. From the image-to-core direction, approximately 91% of fracture features identified on borehole images can be matched to fractures observed in core, whereas approximately 9% have no apparent core counterpart.

By integrating key parameters such as dip angle, cross-layer extension, and spatial position within the borehole, we

established an image response pattern for natural fractures in borehole images. Compared with previous fracture identification results, applying the pattern improved the natural fracture identification rate by 17.2% in water-based mud wells and by 3.4% in oil-based mud wells.

During the fracture identification process, one must understand the bidirectional matching deviations between core fractures and image features, mitigate common pitfalls in natural fracture identification. Only by doing so can we ensure provide a reliable data foundation for exploration and development under complex geological conditions.

CRediT authorship contribution statement

Yu Du: Writing – review & editing, Writing – original draft, Validation, Supervision, Software, Methodology, Formal analysis, Data curation, Conceptualization. **Hu-Cheng Deng:** Supervision, Project administration, Methodology, Investigation, Funding acquisition, Conceptualization. **Xiao-Fei Hu:** Supervision, Software, Methodology. **Hao-Tian Zhang:** Validation, Software, Data curation. **Hong-Hui Wang:** Validation, Methodology. **Cui-Li Wang:** Resources, Data curation. **Mao-Xin Liu:** Visualization. **Chen-Yang Zhao:** Visualization. **Zi-Yun Zheng:** Visualization.

Declaration of competing interest

The authors declare that there have no known competing financial interests or personal relationships that could have appeared to influence the work reported in this paper.

Acknowledgements

This work was supported by the National Natural Science Foundation of China (No. 42072182) and the Science and Technology Department of Sichuan Province (No. 2024NSFSC0815). Meanwhile, this research has been strongly supported by the Natural Gas Development Research Department, Exploration and Development Research Institute, PetroChina Tarim Oilfield Company, and we sincerely appreciate for it.

References

Azizzadeh Mehmandost Olya, B., Mohebian, R., Bagheri, H., Mahdavi Hezaveh, A., Khan Mohammadi, A., 2024. Toward real-time fracture detection on image logs using deep convolutional neural network YOLOv5. Interpretation 12, SB9–SB18. https://doi.org/10.1190/INT-2022-0104.1.

Ballester, C., Bertalmio, M., Caselles, V., Sapiro, G., Verdera, J., 2001. Filling-in by joint interpolation of vector fields and gray levels. IEEE Trans. Image Process. 10, 1200–1211.

Cao, D., Zeng, L., Gomez-Rivas, E., Gong, L., Liu, G., Lu, G., Bons, P.D., 2024. Correction of linear fracture density and error analysis using underground borehole data. J. Struct. Geol. 184, 105152.

Cao, F., He, J., Wang, Y., Deng, H., Xu, Q., 2022. Methods to evaluate present-day in-situ stress direction for low anisotropic reservoirs in the second member of the xujiahe formation in hechuan area. Adv. Earth Sci. 37, 742–755. https://doi.org/10.11867/j.issn.1001-8166.2022.036 (in Chinese).

Chen, D., Wang, C., Deng, H., Chen, N., Ding, H., Hu, X., Zhang, H., Yang, Y., DU, Y., Gao, Y., 2024. Evaluation of characteristics, distribution, and production control of advantageous natural fractures in ultra-deep layers: A case study of the Lower Cretaceous tight sandstone in the bozi-dabei area of the tarim Basin. Nat. Gas Geosci. 1–23. https://doi.org/10.11764/j.issn.1672-1926.2025.07.002 (in Chinese).

Chen, J., Yang, L., Zhao, Y., Zhao, H., Zhang, W., 2021. Application of deep neural network model in processing of electrical logging images. Electron Meas Technol 44, 138–143. https://doi.org/10.19651/j.cnki.emt.2005617.

Chen, Y., Fu, G., Hu, M., Zhang, H., 2017. The quantitative study of structure genetic mechanism about T11 reflecting layer fault in the Sanzhao sag of Songliao Basin. Chinese J Geol 52, 359–374. https://doi.org/10.12017/dzkx.2017.025 (in Chinese).

Chitale, D.V., Quirein, J., Perkins, T., Lambert, G.B., Cooper, J.C., 2004. Application of a new borehole imager and technique to characterize secondary porosity and net-to-gross in vugular and fractured carbonate reservoirs in Permian Basin. SPWLA Annual Logging Symposium. SPWLA-2004-RR.

Deng, H., Zhou, W., Zhou, Q., Chen, W., Zhang, H., 2013. Quantification characterization of the valid natural fractures in the 2nd Xu Member, Xinchang gas fiel. Acta Petrol. Sin. 29, 1087–1097. https://doi.org/10.1007/s13272-013-0078-8 (in Chinese).

Dong, Q., Cao, C., Fu, Y., 2022. Incremental transformer structure enhanced image inpainting with masking positional encoding. Proceedings of the IEEE/CVF conference on computer vision and pattern recognition 11358–11368 (in Chinese).

Dong, S., Zeng, L., Che, X., Du, X., Xu, H., Ji, C., Yang, W., Li, Z., 2023. Application of artificial intelligence in fracture identification using well logs in tight reservoirs. Earth Sci. 48, 2443–2461. https://doi.org/10.3799/dqkx.2022.088 (in Chinese).

Du, L., Lu, X., Li, H., 2023. Automatic fracture detection from the images of electrical image logs using Mask R-CNN. Fuel 351, 128992. https://doi.org/10.1016/j.fuel.2023.128992.

Ekstrom, M.P., Dahan, C.A., Chen, M.-Y., Lloyd, P.M., Rossi, D.J., 1986. Formation imaging with microelectrical scanning arrays. SPWLA Annual Logging Symposium. SPWLA-1986-BB.

Fernandez-Ibanez, F., DeGraff, J., Ibrayev, F., 2018. Integrating borehole image logs with core: a method to enhance subsurface fracture characterization. AAPG (Am. Assoc. Pet. Geol.) Bull. 102, 1067–1090. https://doi.org/10.1306/0726171609317002.

Folkestad, A., Veselovsky, Z., Roberts, P., 2012. Utilising borehole image logs to interpret delta to estuarine system: a case study of the subsurface Lower Jurassic Cook Formation in the Norwegian northern North Sea. Mar. Petrol. Geol. 29, 255–275. https://doi.org/10.1016/j.marpetgeo.2011.07.008.

Fu, Q., 2020. Research of Enhancement and Restoration Method for Ultrasonic Logging Images. Ph.D. thesis (in Chinese).

Gaillot, P., Brewer, T., Pezard, P., Yeh, E.-C., 2007. Borehole imaging tools—principles and applications. Sci. Drill. 5, 1. https://doi.org/10.2204/iodp.sd.5.07S1.2007.

Genter, A., Castaing, C., Dezayes, C., Tenzer, H., Traineau, H., Villemin, T., 1997. Comparative analysis of direct (core) and indirect (borehole imaging tools) collection of fracture data in the Hot Dry Rock Soultz reservoir (France). J. Geophys. Res. Solid Earth 102, 15419–15431. https://doi.org/10.1029/97JB00626.

Goldberg, D., 1997. The role of downhole measurements in marine geology and geophysics. Rev. Geophys. 35, 315–342. https://doi.org/10.1029/97RG00221.

Gong, L., Qin, X., Gao, S., Fu, X., 2024. Multi-scale fracture development characteristics and fracture network patterns of buried-hill in metamorphic rocks: a case study of the Bozhong Z metamorphic buried-hill. Earth Sci. Front. 31, 332–343. https://doi.org/10.13745/j.esf.sf.2024.6.19 (in Chinese).

Goodfellow, I., Pouget-Abadie, J., Mirza, M., Xu, B., Warde-Farley, D., Ozair, S., Courville, A., Bengio, Y., 2014. Generative adversarial nets. Adv. Neural Inf. Process. Syst. 27.

Hall, J., Ponzi, M., Gonfalini, M., Maletti, G., 1996. Automatic extraction and characterisation of geological features and textures front borehole images and core photographs. SPWLA Annu. Logging Symp. SPWLA-1996-CCC.

Han, S., Xiao, X., Song, B., Guan, T., Zhang, Y., Lyu, M., 2023. Automatic borehole fracture detection and characterization with tailored Faster R-CNN and simplified Hough transform. Eng. Appl. Artif. Intell. 126, 107024. https://doi.org/10.1016/j.engappai.2023.107024.

Hu, X., Deng, H., Gao, Y., Du, Y., Wang, C., 2025. Natural fractures differential distribution characteristics and genesis in complex tectonic zone: A case study in the Kuqa Foreland of Tarim Basin. Journal of Chengdu University of Technology (Science & Technology Edition, pp. 1–17 (in Chinese).

Hurley, N.F., Zhang, T., 2011. Method to generate full-bore images using borehole images and multipoint statistics. SPE Reserv. Eval. Eng. 14 (2), 204–214. https://doi.org/10.2118/120671-PA.

Ju, W., Li, C., Ning, W., Tan, X., Liu, J., Wang, Y., Zhao, X., Liang, X., 2025. Quantitative evaluation method of natural fracture penetration and its geological influencing factors. Geotect. Metallogenia 1–12. https://doi.org/10.16539/j.ddgzyckx.2025.00.008 (in Chinese).

Kalathingal, P., Kuchinski, R., 2010. The role of resistivity image logs in deep natural gas reservoirs. SPE Deep Gas Conference and Exhibition. SPE-131721-MS.

Ke, S., 2008. Fully 3D numerical simulation and fracture evaluation model of borehole electrical imaging logging. Sci. Sin. 150–153 doi: CNKI:SUN:JDXK.0.2008-S1-018 (in Chinese).

Khoshbakht, F., Azizzadeh, M., Memarian, H., Nourozi, G., Moallemi, S., 2012. Comparison of electrical image log with core in a fractured carbonate reservoir. J. Petrol. Sci. Eng. 86, 289–296. https://doi.org/10.1016/j.petrol.2012.03.007.

Lai, J., Guiwen, W., Sun, S., Jiang, C., Zhou, L., Zheng, X., Wu, Q., Han, C., 2015. Research advances in logging recognition and evaluation method of fractures in tight sandstone reservoirs. Prog. Geophys. 30, 1712–1724. https://doi.org/10.6038/pg20150426 (in Chinese).

Lai, J., Liu, B.-C., Li, H.-B., Pang, X.-J., Liu, S.-C., Bao, M., Wang, G.-W., 2022a. Bedding parallel fractures in fine-grained sedimentary rocks: Recognition, formation mechanisms, and prediction using well log. Pet. Sci. 19, 554–569. https://doi.org/10.1016/j.petsci.2021.10.017.

Lai, J., Pang, X., Zhao, X., Zhao, Y., Wang, G., Huang, Y., Li, H., Li, Y., 2022b. Typical misunderstandings and scientific ideas in well logging geology research. Nat. Gas. Ind. 42, 31–44. https://doi.org/10.3787/i.issn.1000-0976.2022.07.004.

Lai, J., Su, Y., Xiao, L., Zhao, F., Bai, T., Li, Y., Li, H., Huang, Y., Wang, G., Qin, Z., 2024a. Application of geophysical well logs in solving geologic issues: Past, present

and future prospect. Geosci. Front. 15, 101779. https://doi.org/10.1016/j.gsf.2024.101779.
Lai, J., Wang, G., Fan, Z., Wang, Z., Chen, J., Zhou, Z., Wang, S., Xiao, C., 2017. Fracture detection in oil-based drilling mud using a combination of borehole image and sonic logs. Mar. Petrol. Geol. 84, 195–214. https://doi.org/10.1016/j.marpetgeo.2017.03.035.
Lai, J., Wang, G., Wang, S., Cao, J., Li, M., Pang, X., Han, C., Fan, X., Yang, L., He, Z., 2018. A review on the applications of image logs in structural analysis and sedimentary characterization. Mar. Petrol. Geol. 95, 139–166. https://doi.org/10.1016/j.marpetgeo.2018.04.020.
Lai, J., Xiao, L., Bai, T., Fan, Q., Huang, Y., 2024b. Interpretation and evaluation methods of image logs and their biological applications. Bulletin Geol. Sci. Technol. Inf. 43, 323–340. https://doi.org/10.19509/j.cnki.dzkq.tb20220701.
Laronga, R., Lozada, G.T., Perez, F.M., Cheung, P., Hansen, S.M., Rosas, A.M., 2011. A high-definition approach to formation imaging in wells drilled with nonconductive muds. SPWLA Annu. Logging Symp. SPWLA-2011-FFF.
Li, D., Liu, X., Zhong, G., Guo, X., 2009. Interpretation of imaging logs of sedimentary microfacies of reef-flat reservoir in Tazhong No. 1 slope break zone, Tarim Basin. Xinjing Pet. Geol. 30, 197 (in Chinese).
Li, D., Wang, G.-W., Bie, K., Lai, J., Lei, D.-W., Wang, S., Qiu, H.-H., Guo, H.-B., Zhao, F., Zhao, X., 2025a. Formation mechanism and reservoir quality evaluation in tight sandstones under a compressional tectonic setting: The Jurassic Ahe Formation in Kuqa Depression, Tarim Basin, China. Pet. Sci. 22, 998–1020. https://doi.org/10.1016/j.petsci.2024.12.026.
Li, F., Ni, X., Xu, S., Pan, T., Liu, D., 2025b. Response simulation and detection of LWD azimuthal laterolog resistivity imaging tool in fractured reservoirs. Prog. Geophys. 1–17.
Li, H., Lin, C., Ren, L., Ma, C., Dong, C., Li, S., Liang, S., 2020a. Tectonic fracture prediction based on the coupling constraint of lithofacies and fault damage zone: A case study of the 2ndsand group of middle Es3 member in Daluhu oilfield, Boxing subsag. J. China Univer. Mining.Technol. 49, 305–317+340. https://doi.org/10.13247/j.cnki.jcumt.001129 (in Chinese).
Li, J., Kang, Z., Kang, Z., Liu, X., Zhang, X., 2024. Hydrothermal fluid alteration of the Ordovician epigenetic karstification reservoir in the Tahe Oilfield, Tarim Basin, NW China. Sci. Total Environ. 912, 169363. https://doi.org/10.1016/j.scitotenv.2023.169363.
Li, N., Caizhi, W., Yingming, L., Li, W., Shouji, X., Ye, Y., 2013. CIFLog: The 3rd generation logging software based on Java-NetBeans. Acta Pet. Sin. 34, 192. https://doi.org/10.7623/syxb201301026 (in Chinese).
Li, N., Zou, C., Peng, C., Zhao, J., Niu, Y., 2017a. Core spatial Position restoring of the CCSD-SK-2 east borehole in the Songliao Basin of Northeast China. Geol. Sci. Technol. Inf. 36, 271–276. https://doi.org/10.19509/j.cnki.dzkq.2017.0437 (in Chinese).
Li, Q., Pan, H., Zhang, R., 2005. The progress of resistivity imaging log. Chin. J. Eng. Geophys. 304–310. https://doi.org/10.3969/j.issn.1672-7940.2005.04.010 (in Chinese).
Li, Q., Zhang, H., Qiu, K., Wang, X., Huaung, Z., Du, P., Su, Z., Lei, L., 2020b. Research on the rock drillability prediction methods ol deep strata in the East China Sea. China Offshore Oil Gas 32, 126–133. https://doi.org/10.11935/j.issn.1673-1506.2020.02.015.
Li, R., 2017. Fine logging evaluation of natural fractures in the Keshen 8 ultradeep gas field. Kuqa depression. M.S. thesis (in Chinese).
Li, Z., Shen, J., Li, S., 2017b. Singular spectral interpolation of blank strips in formation micro-scanner conductivity image and separation of porosity between fracture and karst Cave. Well Logging Technol. 41, 33–40. https://doi.org/10.16489/j.issn.1004-1338.2017.01.006 (in Chinese).
Lin, C., Liu, J., Zhang, Y., Xiao, J., Chen, J., Ji, Y., 2002. Depositional architecture of the Tertiary tectonic sequences and their response to foreland tectonism in the Kuqa depression, the Tarim Basin. Sci. China Earth Sci. 45, 250–258. https://doi.org/10.1360/02yd9027.
Liu, Q., Tang, H., Lv, Z., Wang, Q., Liu, Z., 2023. Study on gas-water distribution and water invasion law under different fracture development models in ultra-deep gas reservoir: Taking Keshen 2, 9 and 8 gas reservoirs of Tarim Basin as examples. Nat. Gas Geosci. 34, 963–972. https://doi.org/10.11764/i.issn.1672-1926.2023.01.004 (in Chinese).
Liu, R., Li, J., Xiao, Z., Li, J., Zhang, H., Lu, Y., Zhang, B., Ma, W., Li, D., Liu, M., 2019. Geochemical characteristics and their gas and oil source correlation implication in the Tugeerming area of the Kuqa Depression, Tarim Basin, China. J Nat Gas Geosci 4, 161–168. https://doi.org/10.1016/j.jnggs.2019.06.001.
Liu, Y., 2013. Fracture Characteristics of Low Permeability Reservoirs and the Control Action of the Accumulation of Oil and Gas. Ph.D. thesis (in Chinese).
Liu, Y., 2023. Reservoir Characteristics and Main Controlling Factors of the Cretaceous Bashijiqike Formation in the Bozi-Dabei Area of Kuqa Depression. M.S. thesis (in Chinese).
Liu, Y., Qiu, Y., Feng, Q., 2013. Automated method for picking up sinusoidal shaped geologic formations in imaged logging images. Well Logging Technol. 37, 523–526. https://doi.org/10.16489/j.issn.1004-1338.2013.05.014.
Lofts, J.C., Bristow, J., 1998. Aspects of core-log Integration: an Approach Using High Resolution Images, 136. Geological Society, London, Special Publications, pp. 273–283. https://doi.org/10.1144/GSL.SP.1998.136.01.23.
Luo, Q., Tang, H., Liu, Q., Yin, Y., Lixin, W., Shang, H., 2023. Multi-scale fracture modeling method and its application: A case study of tight sandstone reservoir in Keshen 2 Gas Field, Tarim Basin. Nat. Gas Geosci. 35, 1000–1013. https://doi.org/10.11764/j.issn.1672-1926.2023.11.010 (in Chinese).
Ma, L., Jiang, X., Gong, J., 2022. Analysis of logging characteristics of high quality shale gas reservoirs. Reservoir Eval. and Dev. 12, 445–454. https://doi.org/10.13809/j.cnki.cn32-1825/te.2022.03.006.
MacLeod, C., Parson, L., Sager, W., Party, O.L.S., 1992. Identification of tectonic rotations in boreholes by the integration of core information with Formation MicroScanner and Borehole Televiewer images. Geol. Soc. Lond. Spec. Publ. 65, 235–246. https://doi.org/10.1144/GSL.SP.1992.065.01.18.
Massiot, C., McNamara, D.D., Lewis, B., 2015. Processing and analysis of high temperature geothermal acoustic borehole image logs in the Taupo Volcanic Zone, New Zealand. Geothermics 53, 190–201. https://doi.org/10.1016/j.geothermics.2014.05.010.
Mitchell, B.J., 1995. Anelastic structure and evolution of the continental crust and upper mantle from seismic surface wave attenuation. Rev. Geophys. 33, 441–462. https://doi.org/10.1029/95RG02074.
Nian, T., Wang, G., Fan, X., Tan, C., Wang, S., Hou, T., 2021. Advances in fracture and vug interpretation using microresistivity imaging logs. Geol. Rev. 67, 476–488. https://doi.org/10.16509/j.georeview.2021.02.016 (in Chinese).
Niu, Y., Pan, H., Wang, W., 2005. Spatial Localization of Logging Core in the Main Hole (101~2000 m) of Scientific Drilling on the Chinese Continent, 30. China University of Geosciences Press, pp. 102–107.
Olson, J.E., Laubach, S.E., Lander, R.H., 2009. Natural fracture characterization in tight gas sandstones: Integrating mechanics and diagenesis. AAPG Bull. 93, 1535–1549. https://doi.org/10.1306/08110909100.
Pan, B., Liu, W., Zhang, L., Guo, Y., Aruhan, 2018. A method for improving accuracy of Reservoir fracture identification. J. Jilin Univ. (Sci. Ed.) 48, 298–306. https://doi.org/10.13278/j.cnki.jjuese.20160343.
Pan, L., Du, H., Li, L., Long, T., 2024. Fracture development characteristics and main controlling factors of natural fracture in the Upper Triassic Xujiahe Formation in Yuanba area, Northeastern Sichuan Basin. Earth Sci. Front. 31, 156–165. https://doi.org/10.13745/j.esf.sf.2024.6.12.
Paulsen, T.S., Jarrard, R.D., Wilson, T.J., 2002. A simple method for orienting drill core by correlating features in whole-core scans and oriented borehole-wall imagery. J. Struct. Geol. 24, 1233–1238. https://doi.org/10.1016/S0191-8141(01)00133-X.
Qi, B., He, H., Zhao, N., Xu, H., Zeng, Y., 2025. Extraction and correction of key parameters of carbonate's fracture-vug based on core scale electrical imaging images. Prog. Geophys. 1–13 (in Chinese).
Prensky, S.E., 1999. Advances in borehole imaging technology and applications. Geol. Soc. Lond. Spec. Publ. 159, 1–43. https://doi.org/10.1144/GSL.SP.1999.159.01.01.
Qi, Z., 2005. Research and application of the quantitative processing methods of electric imaging log data. Nat. Gas. Ind. 25, 32. https://doi.org/10.3321/j.issn:1000-0976.2005.06.008.
Qin, J., Xian, C., Wang, W., Li, S., Zhou, F., 2025. Characteristics of hydraulic fracture network in the tight conglomerate reservoir based on a hydraulic fracturing test site. Petrol. Explor. Dev. 52, 245–257. https://doi.org/10.11698/PED.20240580.
Qin, W., Chen, X., 2000. A math-morphological approach for automatic fracture recognition on sidewall images. Well Logging Technol. 25, 64–69. https://doi.org/10.16489/j.issn.1004-1338.2001.01.017 (in Chinese).
Qu, H., Zhang, F., Wang, Z., Yang, X., Liu, H., Ba, D., Wang, X., 2016. Quantitative fracture evaluation method based on core-image logging: A case study of Cretaceous Bashijiqike Formation in ks2 well area, Kuqa depression, Tarim Basin, NW China. Petrol. Explor. Dev. 43, 465–473. https://doi.org/10.1016/s1876-3804(16)30054-4.
Reber, J.E., Lavier, L.L., Hayman, N.W., 2015. Experimental demonstration of a semi-brittle origin for crustal strain transients. Nat. Geosci. 8, 712–715. https://doi.org/10.1038/ngeo2496.
Rumelhart, D.E., Hinton, G.E., Williams, R.J., 1985. Learning Internal Representations by Error Propagation, Institute for Cognitive Science. University of California, San Diego La.
Safinya, K., Le Lan, P., Villegas, M., Cheung, P., 1991. Improved formation imaging with extended microelectrical arrays. SPE Annu. Tech. Conf. Exhib. SPE-22726-MS.
Shafiabadi, M., Kamkar-Rouhani, A., Riabi, S.R.G., Kahoo, A.R., Tokhmechi, B., 2021. Identification of reservoir fractures on FMI image logs using Canny and Sobel edge detection algorithms. Oil & Gas Sci. Technol.–Revue d'IFP Energies nouvelles 76, 10. https://doi.org/10.2516/ogst/2021023.
Su, Y., Lai, J., Bie, K., Li, D., Zhao, F., Chen, K., Li, H., Wang, G., 2025. Well logging evaluation and characterization of geological information for deep and ultra-deep drilling wells. J. Palaeogeogr. 27, 225–239. https://doi.org/10.7605/gdlxb.2024.06.068.
Su, Y., Lai, J., Dang, W., Bie, K., Zhao, Y., Zhao, X., Li, D., Zhao, F., Wang, G., 2024. Pore structure characterization and reservoir quality prediction in deep and ultra-deep tight sandstones by integrating image and NMR logs. J. Asian Earth Sci. 272, 106232. https://doi.org/10.1016/j.jseaes.2024.106232.
Sun, D., Lv, H., Wang, L., Cui, J., He, B., Cao, Z., Qiu, H., Yan, X., 2018. Determination of the in-situ stress state at 7 km depth under Tarim Basin by ASR and DITH methods. Rock Mech. Eng. 37, 383–391. https://doi.org/10.13722/j.cnki.jrme.2016.1145 (in Chinese).
Sun, J., Xiao, H., Yao, Z., 2006. Application of acoustoelectric image-forming logging technique in reservoir frac-ture identification. Pet. Geol. Oilfield Dev. Daqing 25, 100–102. https://doi.org/10.3969/j.issn.1000-3754.2006.03.036.

Sun, Y., 2016. Fracture Recognition Effect Analysis of Different Acoustic and Electric Image Logging in Tight Sandstone Reservoir—Taking Keshen Gas Field as an Example. M.S. thesis (in Chinese).
Tang, J., Zhang, C., Xin, Y., 2017. A fracture evaluation by acoustic logging technology in oil-based mud: A case from tight sandstone reservoirs in Keshen area of Kuqa Depression, Tarim Basin, NW China. Petrol. Explor. Dev. 44, 418–427.
Tang, L., Li, J., Yu, Y., Wang, Q., Yang, W., Xie, H., Chen, S., Peng, G., 2006. Differential salt tectonic deformation and segmentation of the Kuqa Foreland fold-thrust Belt, Tarim Basin, Northwest China. Acta Geol. Sin. 80, 313–320. https://doi.org/10.3321/j.issn:0001-5717.2006.03.001.
Wang, K., Zhang, R., Zeng, Q., Wang, J., Xia, J., Mo, T., 2022a. Characteristics and formation mechanism of lower Cretaceous deep and ultra-deep reservoir in Bozi-Dabei Area, Kuqa Depression Reservoir in Bozi-Dabei Area, Kuqa Depression. Journal of China University of Mining & Technology, 51, 311–328.https://doi.org/10.13247/j.cnki.jcumt.001337 (in Chinese).
Wang, L., Zhen, J., Zou, C., Nie, X., 2014. Core spatial restoring with imaging logging data and effect analysis. Bulletin Geol. Sci. Technol. 33, 207–212 (in Chinese).
Wang, S., Wang, G., Li, D., Wu, X., Chen, X., Wang, Q., Cao, J., Zhang, Y., 2022b. Comparison between double caliper, imaging logs, and array sonic log for determining the in-situ stress direction: A case study from the ultra-deep fractured tight sandstone reservoirs, the Cretaceous Bashijiqike Formation in Keshen8 region of Kuqa depress. Pet. Sci. 19, 2601–2617. https://doi.org/10.1016/j.petsci.2022.08.035.
Wang, S., Wang, G., Zeng, L., Liu, P., Huang, Y., Li, S., Wang, Z., Zhou, Y., 2025. New method for logging identification of natural fractures in shale reservoirs: The Fengcheng Formation of the Mahu Sag, China. Mar. Petrol. Geol. 176, 107346. https://doi.org/10.1016/j.marpetgeo.2025.107346.
Wang, W., 2023. Study on Tectonic Evolution and Fracture Development Characteristics of Archean Metamorphic Buried Hill in Bohai Sea. Ph.D. thesis (in Chinese).
Wang, Z., Gao, N., Zeng, R., Du, X., Du, X., Chen, S., 2019. A gaps filling method for electrical logging images based on a deep learning model. Well Logging Technol. 43, 578–582. https://doi.org/10.16489/j.issn.1004-1338.2019.06.005 (in Chinese).
Wang, Z., Wang, C., Xu, K., Zhang, H., Chen, N., Deng, H., Hu, X., Yang, Y., Feng, X., Du, Y., 2023. Characteristics and control factors of tectonic fractures of ultra-deep tight sandstone: Case study of the Lower Cretaceous reservoir in Bozi-Dabei area, Kuqa Depression, Tarim Basin, China. J Nat Gas Geosci 8, 439–453. https://doi.org/10.11764/i.issn.1672-1926.2023.05.006.
Wood, D.A., 2024. Expanding role of borehole image logs in reservoir fracture and heterogeneity characterization: A review. Adv. Geo-Energy Res. 12, 194–204. https://doi.org/10.46690/ager.2024.06.04.
Wu, X., Yan, T., Jj, F., 2007. The coring and sampling technology under complicated geological condition. Coal Geol. Explor. 35, 73–76 (in Chinese).
Wu, Y., Li, H., Song, Y., 2016. Nonlocal means image denoising Algorithm based on steering kernel clustering. J. Univ. Electron. Sci. Technol. China 45, 36–42. https://doi.org/10.3969/i.issn.1001-0548.2016.01.005 (in Chinese).
Xavier, A., Guerra, C.E., Andrade, A., 2015. Fracture analysis in borehole acoustic images using mathematical morphology. J. Geophys. Eng. 12, 492–501. https://doi.org/10.1088/1742-2132/12/3/492.
Xu, K., Yang, H., Zhang, H., Ju, W., Li, C., Fang, L., Wang, Z., Wang, H., Yuan, F., Zhao, B., 2022. Fracture effectiveness evaluation in ultra-deep reservoirs based on geomechanical method, Kuqa Depression, Tarim Basin, NW China. J. Petrol. Sci. Eng. 215, 110604. https://doi.org/10.1016/j.petrol.2022.110604.
Xue, Y., Lyu, D., Hu, Z., Huang, J., Ren, J., 2021. Tectonic development of subtle faults and exploration in mature areas in Bohai Sea, East China. Petrol. Explor. Dev. 48, 269–285. https://doi.org/10.1016/S1876-3804(21)60022-8.
Yamada, T., Quesada, D., Etchecopar, A., Le Nir, I., Delhomme, J.-P., Russel-Houston, J., Perdana, T.S.P., 2013. Revisiting porosity analysis from electrical borehole images: Integration of advanced texture and porosity analysis. SPWLA Annual Logging Symposium. SPWLA-2013-E.
Yan, J., Shou, X., Shao, Z., Yao, S., Zhao, Z., 2006. The method of image dynamic intensify and morphing in imaging log. Well Logging Technol. 30, 364. https://doi.org/10.16489/j.issn.1004-1338.2006.04.022.
Yang, H., Hu, T., Yu, H., 2008. Seismic reservoir prediction of reef-flat complexes in the Upper Ordovician, Tazhong area. Oil Gas Geol. 29, 230–236.
Yao, R., Wang, P., Song, L., Tang, H., Bai, B., 2011. Imaging logging response to volcanic pores and fractures of Yingcheng Formation in the Songliao Basin. Prog. Geophys. 26, 2122–2131. https://doi.org/10.3969/j.issn.1004-2903.2011.06.029 (in Chinese).
Ye, D., Liu, G., Wang, F., Gao, F., Yang, T., Zhu, J., 2023. Fractal hydrological-thermal–mechanical analysis of unconventional reservoir: A fracture-matrix structure model for gas extraction. Int. J. Heat Mass Tran. 202, 123670. https://doi.org/10.1016/j.ijheatmasstransfer.2022.123670.
You, Z., Du, X., Hou, H., Zhou, K., Zhang, F., 2000. Discussion on imaging log interpretation mode. Well Logging Technol. 393–399. https://doi.org/10.16489/j.issn.1004-1338.2000.05.016 (in Chinese).
Yuan, X., Ma, X., Xiao, S., Deng, Z., Muladili, M., 2022. A deep neural network method for filling blank strips in electrical logging images based on fusion of multi-level semantic features. J. Xi'an Shiyou Univer. (Nat. Sci. Ed.) 37, 133–139. https://doi.org/10.3969/i.issn.1673-064X.2022.06.018 (in Chinese).
Zeng, L., Gong, L., Guan, C., Zhang, B., Wang, Q., Zeng, Q., Lyu, W., 2022. Natural fractures and their contribution to tight gas conglomerate reservoirs: A case study in the northwestern Sichuan Basin, China. J. Petrol. Sci. Eng. 210, 110028. https://doi.org/10.1016/j.petrol.2021.110028.
Zeng, L., Ma, S., Tian, H., Xue, M., Liu, G., Lyu, W., 2023a. Research progress of natural fractures in organic rich shale. Earth Sci. 48, 2427–2442. https://doi.org/10.3799/dqkx.2022.190 (in Chinese).
Zeng, L., Song, Y., Liu, G., Tan, X., Xu, X., Yao, Y., Mao, Z., 2023b. Natural fractures in ultra-deep reservoirs of China: A review. J. Struct. Geol., 104954 https://doi.org/10.1016/j.jsg.2023.104954.
Zhang, G., 2013. Principle and image acquisition of core imaging technology. Mud Logging Eng. 24, 37–40+91 (in Chinese).
Zhang, G., Zhang, B., Xu, K., Shen, C., Zhang, H., Yin, G., Wwang, H., Wwang, Z., Liu, J., 2024. Fracture characteristics of ultra-deep tight sandstone reservoirs in the Bozi Block, Kuqa Depression of Tarim Basin, and effects on oil-gas production. Bulletin Geol. Sci. Technol. 43, 75–86. https://doi.org/10.19509/j.cnki.dzkq.tb20220454 (in Chinese).
Zhang, R., Yang, H., Wang, J., Shou, J., Zeng, Q., Liu, Q., 2014. The formation mechanism and exploration significance of ultra-deep, low-porosity and tight sandstone reservoirs in Kuqa depression, Tarim Basin. Acta Pet. Sin. 35, 1057. https://doi.org/10.7623/syxb201406003 (in Chinese).
Zhang, X., Pan, B., 2012. Two-dimensional wavelet transform to identify fractures in imaging logging. Shiyou Diqiu Wuli Kantan 47, 173–176. https://doi.org/10.13810/j.cnki.issn.1000-7210.2012.01.001 (in Chinese).
Zhao, Z., Xu, W., Zhao, Z., Yi, S., Yang, W., Zhang, Y., 2024. Geological characteristics and exploration breakthroughs of coal rock gas in Carboniferous Benxi Formation, Ordos Basin, NW China. Petrol. Explor. Dev. 51, 234–247+259. https://doi.org/10.11698/PED.20230679.
Zhong, Y., Dong, S., Liu, K., 2018. Technique of use imaging logging date to complete the classification of microfacies. Nat. Natural Gas Acad 799–806. https://doi.org/10.26914/c.cnkihy.2018.002954 (in Chinese).
Zhu, G., Zhang, Z., Zhou, X., Li, T., Han, J., Sun, C., 2019a. The complexity, secondary geochemical process, genetic mechanism and distribution prediction of deep marine oil and gas in the Tarim Basin, China. Earth Sci. Rev. 198, 102930. https://doi.org/10.1016/j.earscirev.2019.102930.
Zhu, Z., Wu, X., Dong, X., Cao, L., He, G., 2019b. Large diameter coring technology for shale oil exploration in Songliao Basin. Drill. Eng. 46, 45–50 (in Chinese).